Methane depletion in both polar regions of Uranus inferred from HST/STIS† and Keck/NIRC2 observations

L. A. Sromovsky[a], E. Karkoschka[b], P. M. Fry[a], H. B. Hammel[c,d], I. de Pater[e], and K. Rages[f]

Email: larry.sromovsky@ssec.wisc.edu

[a] Space Science and Engineering Center, University of Wisconsin, Madison, WI 53706, USA

[b]University of Arizona, Tucson AZ, USA

[c]AURA, 1212 New York Ave. NW, Suite 450, Washington, DC 20005, USA

[d]Space Science Institute, Boulder, CO 80303, USA

[e]University of California, Berkeley, CA 94720, USA

[f]SETI Institute, Mountain View, CA 94043, USA

Submitted to *Icarus* on 9 January 2014

Manuscript pages: 49 (including references)

Tables: 5

Figures: 30

† Based in part on observations with the NASA/ESA Hubble Space Telescope obtained at the Space Telescope Science Institute, which is operated by the Association of Universities for Research in Astronomy, Incorporated under NASA Contract NAS5-26555.

Proposed Running Head: Polar methane depletion on Uranus

Editorial correspondence to:

Lawrence A. Sromovsky

Space Science and Engineering Center

University of Wisconsin - Madison

1225 W. Dayton Street

Madison, WI 53706

Phone: 608 263-6785

Fax: 608 262-5974

Abstract

Space Telescope Imaging Spectrograph (STIS) observations of Uranus in 2012, when good views of its north polar regions were available, provide constraints on the methane distribution in its northern hemisphere that can be compared with results obtained from similar observations made in August 2002, when good views of its southern hemisphere were obtained. We find that methane depletion in the north polar region of Uranus in 2012 was similar in magnitude and depth to what was found in the south polar regions in 2002. This similarity is remarkable because of the strikingly different appearance of clouds in the two polar regions: the south region has never exhibited any obvious convective activity, while the north has been peppered with numerous small clouds thought to be of convective origin. Keck and HST imaging observations close to equinox at wavelengths with different sensitivities to methane and hydrogen absorption, but similar vertical contribution functions, imply that the depletions were simultaneously present in 2007, and at least its gross character is probably a persistent feature of the Uranus atmosphere. The depletion appears to be of limited depth, with the depth increasing poleward from about 30°. The latitudinal variations in degree and depth of the depletions are important constraints on models of meridional circulation. Our observations are qualitatively consistent with previously suggested circulation cells in which rising methane-rich gas at low latitudes is dried out by condensation and sedimentation of methane ice particles, transported to high latitudes at low pressures, where it descends to higher pressures, bringing down methane depleted gas, which then gets mixed with methane-rich gas on its return flow. Since this cell would seem to inhibit formation of condensation clouds in regions where clouds are actually inferred from spectral modeling, it suggests that sparse localized convective events may be important in cloud formation. A more complex three-layer circulation pattern provides more opportunities for condensation cloud formation, but it also would inhibit convection in some regions where cloud particles are inferred and would seem to conflict with microwave observations which are most compatible with a single deep circulation cell. The small-scale latitudinal variations we found

in the effective methane mixing ratio between 55° N and 82° N have significant inverse correlations with zonal mean latitudinal variations in cloud brightness in near-IR Keck images taken before and after the HST observations, which might be a result of locally reduced methane absorption making clouds appear to be brighter in those regions. While there has been no significant secular change in the brightness of Uranus at continuum wavelengths between 2002 and 2012, there have been significant changes at wavelengths sensing methane and/or hydrogen absorption, with the southern hemisphere darkening considerably between 2002 and 2012, by ∼25% at mid latitudes near 827 nm, for example, while the northern hemisphere has brightened by ∼25% at mid latitudes at the same wavelength.

Key Words: Uranus, Uranus Atmosphere

1 Introduction

Uranus experiences the solar system's largest fractional seasonal forcing because its spin axis has a 98° inclination to its orbital plane. It is thus not surprising to see a time-dependent north-south asymmetry in Uranus' cloud structure. An especially interesting asymmetry noted by Sromovsky et al. (2012) is the continued complete absence of discrete cloud features south of 45° S, while numerous discrete cloud features have been observed north of 45° N in recent near-IR H-filter Keck images (Fig. 1). Some mechanism appears to be inhibiting convection at high southern latitudes that is not present at high northern latitudes. A very significant and possibly related result came from analysis of 2002 Space Telescope Imaging Spectrometer (STIS) observations by Karkoschka and Tomasko (2009), subsequently referenced as **KT2009**, and confirmed by the analysis of Sromovsky et al. (2011). They found a strong depletion of methane in the upper troposphere at high southern latitudes, suggesting a downwelling flow at these latitudes, which would tend to inhibit convective cloud formation. This raised the possibility of a connection between methane depletion and a lack of discrete cloud features, suggesting that high northern latitudes, where discrete clouds are seen, might not be depleted in methane. If, so the methane depletion might be a seasonal effect. In 2002, five years before equinox, the north polar region was not visible, so that testing this hypothesis would require new observations when the north polar region was exposed to view. We thus proposed new STIS observations of Uranus, which were obtained in late September 2012 (HST program 12894, Sromovsky, PI), five years after equinox. The analysis of these new observations is the primary topic in what follows.

[Figure 1 about here.]

Constraining the mixing ratio of CH_4 on Uranus is based on differences in the spectral absorption of CH_4 and H_2, illustrated by the penetration depth plot of Fig. 2A. Methane absorption dominates at most wavelengths, but hydrogen's Collision Induced Absorption (CIA) is relatively more important in

a narrow spectral range near 0.825 μm. Model calculations that don't have the correct ratio of methane to hydrogen lead to a relative reflectivity mismatch near this wavelength. An example is shown in Fig. 2B-D, in which model calculations are compared to 2002 STIS observations assuming methane profiles with 2.2% and 4.0% deep volume mixing ratios. The two assumptions lead to very different errors in the vicinity of 825 nm, clearly indicating that the larger mixing ratio is a better choice. Karkoschka and Tomasko (2009) used this spectral constraint to infer a methane mixing ratio of 3.2% at low latitudes, but dropping to 1.4% at high southern latitudes. Sromovsky et al. (2011) analyzed the same data set, but used only temperature and mixing ratio profiles that were consistent with the Lindal et al. (1987) refractivity profiles. They confirmed the depletion but inferred a somewhat higher mixing ratio of 4% at low latitudes and found that better fits were obtained if the high latitude depletion was restricted to the upper troposphere (down to $\sim$2-4 bars). Subsequently, 2009 groundbased spectral observations with SpeX, which provided coverage of the key 825-nm spectral region, were used by Tice et al. (2013) to infer that both polar regions were weakly depleted in methane, but they inferred lower methane mixing ratios and smaller latitudinal variations than the STIS-based analysis of KT2009 and Sromovsky et al. (2011).

[Figure 2 about here.]

In the following we begin with a description of our 2012 HST/STIS observations, and the complex data reduction and calibration procedures. We then describe the relatively direct implications of latitudinal spectral variations and simplified model results. Finally, we describe our radiation transfer calculation methods and the results of constraining the cloud structure and methane distributions to fit the observed spectra. We show that the methane depletion is indeed present in both polar regions but of significantly different character. The results provide no obvious explanation for the asymmetry in polar cloud structure, but do raise some important questions about cloud formation. The important implications for meridional circulation models are discussed before summarizing our results.

2 Observations

2.1 Overview.

Our 2012 observations used four HST orbits as summarized in Table 1. Three orbits were devoted to STIS observations using the G430L and G750L gratings and the CCD detector, which has ∼0.05 arcsecond square pixels covering a nominal $52'' \times 52''$ square field of view (FOV) and a spectral range from ∼200 to 1030 nm (Hernandez et al. 2012). Using the $52'' \times 0.1''$ slit, the resolving power varies from 500 to 1000 over each wavelength range due to fixed wavelength dispersion of the gratings. The fourth orbit was devoted to WFC3 imaging of the planet with eleven different filters at a pixel scale of 0.04 arcseconds to constrain the absolute calibration of the spectra. Observations had to be carried out within a few days of Uranus opposition (29 September 2012) when the telescope roll angle could be set to 300° or 120° to orient the STIS slit parallel to the spin axis of Uranus. The E1 aperture, which is close to the readout amplifiers, was used to maximize Charge Transfer Efficiency (CTE). The STIS observations were taken on 27-28 September 2012 and the WFC3 observations on 30 September 2012. Observing conditions and exposures are summarized in Table 1.

[Table 1 about here.]

2.2 STIS spatial mosaic design.

One STIS orbit produced a mosaic of half of Uranus using the CCD detector, the G430L grating, and $52'' \times 0.1''$ slit. The G430L grating covers 290 to 570 nm with a 0.273 nm/pixel dispersion. The slit was aligned with Uranus' rotational axis, and stepped from one limb to the central meridian in 0.152 arcsecond increments (because the planet has no high spatial resolution center-to-limb features at these wavelengths we used interpolation to fill in missing columns of the mosaic). Two additional STIS orbits were used to mosaic the planet with the G750L grating and $52'' \times 0.1''$ slit (524-1027 nm coverage with 0.492 nm/pixel dispersion), with limb to central meridian stepping at 0.0569 arcsecond intervals. This

was the same procedure that was used successfully for HST program 9035 in 2002 (E. Karkoschka, P.I.). As Uranus' equatorial radius was 1.85 arcseconds when observations were performed, stepping from one pixel in advance of the central meridian to just off the limb required 13 positions for the G430L grating (at 0.152 arcseconds/step) and 36 for the G750L grating (at 0.0569 arcseconds/step).

Exposure times were similar to those used in the 2002 program, with 70-second exposures for G430L and 86-second exposures for G750L gratings, using the 1 electron/DN gain setting. These exposures yielded single-pixel signal-to-noise ratios of around 10:1 at 300 nm, $>$ 40:1 from around 400 to 700 nm, and decreasing to around 20:1 (methane windows) to $<$ 10:1 (methane absorption bands) at 1000 nm.

2.3 Supporting WFC3 imaging.

Since STIS images can be radiometrically calibrated for point sources or infinitely-extended sources, and Uranus is neither, an empirically determined correction function must be applied to the images as a function of wavelength. This function was determined for the 2002 STIS observations using WFPC2 images of Uranus taken around the same time as the 2002 STIS Uranus observations. To ensure that this function is determined as well as possible for the Cycle 20 observations in 2012, and to cross check the extensive spatial and spectral corrections that are required for STIS observations, we used one additional orbit of WFC3 imaging at wavelengths spread over the 300-1000 nm range of the STIS spectra. These WFC3 images are displayed in Fig. 3, along with synthetic STIS images. The filters and exposures are provided in Table 1. The STIS data cubes were used to create synthetic band-pass filter images matching the spectral weighting of the WFC3 observations, as shown in Fig. 3, and then compared to WFC3 observations to check and revise the STIS spectral calibration. In both WFC3 and synthetic images, the effects of the epsilon ring can be seen as a dark band the F467M image, appearing about 2/3 of the way from the center of the disk to the southern (left) limb. The ring obscuration is largely filled in by image blur and causes a relatively small depression of $\sim$1.5%. The ring albedo is too low to provide

significant reflective contributions except at wavelengths for which the atmosphere is also very dark (in the near-IR deep methane or hydrogen bands).

[Figure 3 about here.]

3 Data reduction and calibration.

The STIS pipeline processing used at STScI does not yield suitably calibrated two-dimensional spectral images for an object like Uranus. The considerable additional effort to reach a final calibration of these data was developed by KT2009 and closely followed in the calibration of the 2012 STIS observations. Flat-fielded science images, fringe flats, and wavecals from the STScI STIS data processing pipeline are the inputs to a rather extensive post-processing suite, the result of which is a cube of geometrically and radiometrically calibrated monochromatic images of Uranus.

3.1 Data reduction

The basic steps of data reduction are as follows.

(1) *Interpolation of bad pixels and cosmic ray hits.* First, images were cleaned of pixels affected by cosmic rays and other defects. An automated routine found 44,000 bad pixels. These were checked to verify that the routine never found any real features. However, along the edges of big cosmic ray events, sometimes covering 100 pixels, the routine is conservative. If slightly elevated counts can be real, they are identified as good pixels and thus used to interpolate across the bad pixels, which then end up with counts 1 or 2 sigma above the background.

(2) *Flat-fielding.* Long wavelength fringing must be removed from G750L spectral images via division by normalized fringe flats (taken contemporaneously with Uranus science observations). For the “red” wavelength range (covered by the 750L grating), the two acquired flat-fields were averaged and the slow wavelength dependent variation was taken out. This gave the fringes and the variation due to variable slit

width along the slit. This flat field was used for the red-range data. Averaging in wavelength was used to obtain the slit variation only and we shifted it vertically (along the slit) by almost one pixel to obtain a flat field for the "blue" wavelength range, which is not affected by fringing. Remaining east-west streaks (perpendicular to the slit) for the blue range were measured, and the blue flat field was changed by 0.1% RMS. There are still very low-contrast streaks remaining, but the results are considered acceptable. A correction is then applied for slit throughput as a function of image row.

(3) *Charge transfer efficiency corrections.* Next a column-by-column deconvolution is performed to correct for Charge Transfer Efficiency (CTE) losses. The previous method of KT2009 was used but the charge loss was adjusted so that resulting images would show counts in space that were roughly symmetric (above and below Uranus). We did not achieve perfect symmetry for all wavelengths simultaneously since charge transfer is very complicated.

(4) *Scattered light corrections.* A spectral image deconvolution was performed to reduce the effects of the "Red Halo" CCD substrate scattering, again following KT2009.

(5) *Distortion correction.* Spectral lines are curved and not vertical, and spectra of the same location are curved and not horizontal. This distortion was removed according to published STScI parameters (Bostroem and Proffitt 2011), except that the first-order terms were adjusted according to measurements on the 2012 spectral calibration data.

(6) *Spectral calibration.* Zero- and first order terms of the function describing wavelength locations on the detector were measured for each exposure. Second-order terms were from STScI (Walsh et al. 2001). For the blue range, 7 Fraunhofer lines were measured, and they stayed constant within 0.01 pixel RMS for the 13 exposures. For the red range, 2 Fraunhofer lines were measured, and they moved by 0.12 pixels (0.06 nm) within the two hours. The red shift due to rotation of Uranus was taken into account based on the location probed, due to the changing distance Earth-Uranus, and due to HST's orbit around Earth. Vacuum wavelengths were used for calibration (since HST is in vacuum). Note that

the longest wavelength sharp spectral feature measurable is the H-alpha Fraunhofer line. Thus, much beyond 656 nm, the wavelength calibration is not as reliable as below. However, since spectral features at long wavelengths are not very sharp (compared to short-wavelength Raman features, for example), it is not as critical there.

(7) *Spectral resolution adjustment.* The blue range was smoothed and the red range was slightly sharpened (rapid variations with wavelength were enhanced) to obtain 1 nm resolution throughout. We took into account that spectra are sharper near the limb of Uranus because the slit is not evenly illuminated.

(8) *Navigation.* The red-range data were convolved with the spectral sensitivity distribution of the acquisition image and then each slit was moved in both axes to obtain the best fit. For the data far from the limb and central meridian, there is a linear trend in best-fit slit position up to about 0.04 pixels RMS (except a 0.2-pixel jump during occultation by Earth), which we adopted. This trend was then extrapolated toward the central meridian and toward the limb because navigation there is less accurate. Finally, the red-range navigation was adjusted using data in deep methane bands, where the bright ring around the limb allows accurate navigation. Navigation of the blue range was done by comparing profiles with the red range in the overlapping spectral region.

(9) *Interpolation of blue range.* The same east-west interpolation was used as for the 2002 data to produce 0.05″ sampling from the 0.15″ east-west actual sampling. It is a cubic interpolation, near the center mostly east-west, near the limb mostly parallel to the limb.

(10) *Spatial resampling.* The data cube has 1800 wavelengths from 300.4 to 1020 nm and 75×150 pixels spaced by $0.015 \times R_U$, where R_U = 25559 km, the equatorial radius of Uranus (Seidelmann et al. 2002). This provides an angular scale 0.0277″/pixel compared to the along-slit pixel scale of 0.05″ and the 0.0569″ per scan step from center to limb. This sub-sampling was used to reduce quantization errors associated with pointing changes during spatial scans. It also matches the sub-sampling used by KT2009 and thus facilitates direct comparisons. The right-most column goes along the central meridian, and the

75th pixel counting from the south is the center of the disk. Cubic interpolation was used throughout. (11) *Deconvolution of PSF.* A final deconvolution is then performed to reduce the effects of the telescope diffraction, using monochromatic PSFs generated by tiny tim (Krist 1995). The tiny-tim PSF was used for each wavelength to take out features of the HST PSF. The deconvolved images should have the same PSF for all wavelengths shown in Table 2, where all counts add up to 100,000. This PSF is for the final data sampled at 0.015 x 25559 km (the equatorial radius R_U of Uranus). Model I/Fs with 0.015 R_U sampling and convolved with this PSF should be comparable to the deconvolved spectral data cube provided in supplemental material.

[Table 2 about here.]

3.2 Albedo calibration.

We combined blue and red ranges using the same method as for the 2002 data; we used the blue-range shortward of 530 nm and the red-range longward of 540 nm, with a linearly sliding weighted average in between. The STIS observations of extended sources can be converted to physical units (radiance) with accepted throughput tables. These values can be converted to I/F using a solar flux spectrum (Colina et al. 1996) and the sun-Uranus distance. Unfortunately, the HST STIS pipeline calibration for extended source surface brightness is only valid for objects much larger in apparent size than Uranus ($>$ 60 arcseconds diameter). To overcome this difficulty, we acquired WFC3 images of Uranus close in time to the STIS images (Table 1). The WFC3 images were deconvolved with tiny tim PSFs that were 6x6 arcseconds in size, and reconvolved with an approximation of the PSF given in Table 2. They were then converted to I/F using header PHOTFLAM values and the Colina et al. (1996) solar flux spectrum, averaged over the WFC3 filter bandpasses. The planet's light was integrated out to 1.1 equatorial radii and averaged over the planet's cross section in pixels, computed using NAIF ephemerides (Acton 1996) and spicelib limb ellipse model. The disk-averaged I/F was also computed

for each of the STIS monochromatic images, and the filter- and solar flux-weighted I/F was computed for each of the WFC3 filter passbands that we used.

By comparing the uncalibrated STIS synthetic disk-averaged I/F to the corresponding WFC3 values, we constructed a correction function to radiometrically calibrate the STIS cube. Figure 4 shows the ratios of STIS to WFC3 disk-integrated brightnesses, and the quadratic function that we fit to these ratios as a function of wavelength. Note that the FQ937N ratio fell far off the curve, and was not included in the fit. Figure 4 also shows the function that was used to radiometrically calibrate the 2002 STIS data by KT2009. Whether the difference in functions is due to a true STIS instrument change or due to a difference in filters used in the two calibrations (2002 data were calibrated using WFPC2 images of Uranus) is unknown.

[Figure 4 about here.]

3.3 End-to-end comparisons

As a sanity check on the STIS processing we compared line scans across WFC3 images to the corresponding scans across synthetic WFC3 images created from our calibrated STIS data cubes. The results are shown in Figs. 5. The worst discrepancies are obtained for μ=0.3 (the lower left pair of plots), where the I/F of the synthetic image exceeds that of the WFC3 image for almost every filter. Ratio images in Fig. 3 show that the STIS synthetic images have relatively brighter limbs than the WFC3 images. Part of the discrepancy might arise from the relatively sparse STIS spatial sampling of the shorter wavelengths, which is 0.152 arcseconds in the center-to-limb stepping of the slit, and thus these wavelengths are subject to greater interpolation errors than WFC3, which has a uniform spatial sampling of 0.04 arcseconds per pixel. However, that is not the whole story because substantial I/F biases at $\mu = 0.3$ are also present at longer wavelengths. The calibration procedure has apparently resulted in STIS images with consistently sharper limbs, and limb profiles show more ringing than WFC3 images, including negative values

off the edge of the disk. The net result is that the STIS I/F values at $\mu = 0.3$ need to be reduced by 4-12% to be compatible with WFC3 values. The latitudinal average ratios of STIS to WFC3 I/F values at $\mu = 0.3$ yield an average over all filters (except the FQ937N) of 1.08 with a standard deviation of 0.02. An overall multiplication of STIS I/F values at $\mu = 0.3$ by 0.925 would make all filters agree within 3%, and most within 2%, again excepting the FQ937N filter. However, we did not apply this correction in the following analysis because we found from test calculations that it decreased the fit quality, while not changing the fit parameters by more than their uncertainties. The WFC3 F937M image is brighter at all zenith angles than the corresponding synthetic image obtained from STIS observations. This is a result of the same calibration discrepancy displayed in Fig. 4.

[Figure 5 about here.]

3.4 Center-to-limb fitting

Center-to-limb profiles provide important constraints on the vertical distribution of cloud particles as well as the vertical variation of methane compared to hydrogen. Because Uranus has a high degree of zonal uniformity, these profiles are fairly smooth functions that can be characterized by a small number of parameters, making it possible to constrain the profiles accurately, reducing the effects of noise and skipping over any small discrete cloud features. Because the observations were taken very close to zero phase angle these functions are almost perfectly symmetric about the central meridian, so that they depend on only one cosine value (observer and solar zenith angles are essentially equal). This is also a reason we were able to characterize these profiles by measuring only one half of the Uranus disk.

The true center-to-limb profile is depressed near the limb by the blur of the imaging system. To avoid having to create, for every model calculation, a synthetic disk that could then be convolved with the imaging system PSF so that a model could be compared with the observed profile, we instead applied a crude correction. We created a synthetic planetary disk of unit I/F, convolved that disk with the PSF

kernel used in reconvolving the deconvolved measured images, then computed the ratio of the perfect disk to the convolved synthetic disk. That produced a correction factor, which we applied to the observed I/F values prior to carrying out fits to each center-to-limb profile. The correction is negligible for zenith angle cosines greater than or equal to 0.3.

Center-to-limb fitting took approximate account the two-way transmission of the rings of Uranus, which produces about a 1.5% depression in I/F at the center of the epsilon ring (this depression can be barely seen in the F467M image in Fig. 3). We determined a correction function to reduce the ring's obscuration effects on center-to-limb fits. We started with a simulated F467M image, produced by a weighted average of monochromatic STIS images, as described Sec. 2.3. A ring transmission map was created by starting with all pixels set to unity. The pixels at the ring location (French et al. 1986) were set to a trial transmission value then the map was blurred with a Gaussian of a trial FHWM value. The simulated F467M image was then divided by this correction image. The ring transmission and FWHM values were empirically adjusted until the ring was no longer visible in a high-pass filtered version of the F467M image. The best fit values were roughly 0.935 and 4.5 pixels respectively. We ignored reflecting ring light because ring albedo is so low that reflected light contributions are not apparent at CCD wavelengths.

Before fitting the center-to-limb (CTL) profile for each wavelength, the spectral data are smoothed in the wavenumber domain to a resolution of 36 cm^{-1}, which equals the resolution we use in computing the Raman spectrum, but is four times finer than the sampling we use in constraining cloud models. The effect of this smoothing is quite substantial at the longer wavelengths, as demonstrated in Fig. 6. For each 1° of latitude from 54° S to 85° N, all image samples within 1° of the selected latitude and with $\mu > 0.175$ are collected and fit to the empirical function

$$I(\mu) = a + b\mu + c/\mu, \tag{1}$$

assuming all samples were collected at the desired latitude and using the μ value for the center of each

pixel of the image samples. Sample fits are provided in Figs. 7. Most of the scatter about the fitted profiles is due to noise, which is often amplified by the deconvolution process. The exception appears at 41° N where a large deviation near μ=0.87 is produced by a small discrete cloud feature. Because the range of observed μ values decreases away from the equator at high southern and northern latitudes, latitudinal comparisons at high μ values in those regions rely on uncertain extrapolations.

[Figure 6 about here.]

[Figure 7 about here.]

The CTL fits can also be used to create zonally smoothed images by replacing the observed I/F for each pixel by the fitted value. Results of that procedure are displayed for six sample wavelengths in Fig. 8. Note that the image for the H_2 CIA dominated wavelength (826.8 nm) shows much more equator-to-pole darkening than the image for the methane-dominated wavelength of 833.7 nm, implying that there is relatively less methane absorption (compared to H_2 absorption) at high latitudes. This implication is based on the fact that the two wavelengths are roughly sensitive to the same pressure range and thus are not sensing grossly different aerosol contributions.

[Figure 8 about here.]

4 Direct comparison of methane and hydrogen absorptions vs. latitude.

If methane and hydrogen absorptions had the same dependence on pressure, then it would be simple to estimate the latitudinal variation in their relative abundances by looking at the relative variation in I/F values with latitude for wavelengths that produce similar absorption at some reference latitude. Although this idea is compromised by different vertical dependencies in absorption, which means that latitudinal variation in the vertical distribution of aerosols can also play a role, it is nevertheless useful in a semi-quantitative sense. Thus we explore several cases below.

4.1 Direct comparison of key near-IR wavelength scans in 2007

Our first example is based on a comparison of HST measurements using an F108N filter (1080 nm), which is dominated by H_2 CIA, with KeckII/NIRC2 measurements using a PaBeta filter (1271 nm), which is completely dominated by methane absorption. That these sense roughly the same level in the atmosphere is demonstrated by the penetration depth plot in Fig. 9, which also displays the filter transmission functions. The I/F profiles for these two filters near the 2007 Uranus equinox are displayed in Fig. 10 for μ=0.4 and μ=0.6. These are plotted as true I/F values (not scaled in any way). At high latitudes in both hemispheres, and at both zenith angle cosines, the two profiles agree with each other quite closely and are both increasing towards the equator. But at low latitudes, the profile for the hydrogen-dominated wavelength continues to increase, while the profile for the methane-dominated wavelength decreases substantially, indicating that methane absorption is much higher at low latitudes than at high latitudes.This suggests that upper tropospheric methane depletion (relative to low latitudes) was present at both northern and southern high latitudes in 2007, at least roughly similar to the pattern that was inferred by Tice et al. (2013) from analysis of 2009 SpeX observations.

[Figure 9 about here.]

[Figure 10 about here.]

4.2 Direct comparison of key STIS wavelength scans

A similar spectral comparison of the 2012 STIS observations can also be informative. By selecting wavelengths that at one latitude provide similar I/F values but very different contributions by H_2 CIA and methane, one can then make comparisons at other latitudes to see how I/F values at the two wavelengths vary with latitude. If aerosols did not vary at all with latitude, then this would be a clear measure of the ratio of CH_4 to H_2. Fig. 11 displays a detailed view of I/F spectral region where hydrogen CIA exceeds methane absorption (see Fig. 2 for penetration depths). Near 930 nm and 827 nm the I/F values are

similar but the former is dominated by methane absorption and the latter by hydrogen absorption. Near 835 nm there is a relative minimum in hydrogen absorption, while methane absorption is still strong. At 50° N latitude and μ=0.6, I/F values are nearly the same at all three wavelengths, suggesting that they all produce roughly the same attenuation of the vertically distributed aerosol scattering. At low latitudes, as shown in Fig. 12A, the I/F for the hydrogen-dominated wavelength increases, while the I/F for the methane-dominated wavelength decreases substantially, indicating an increase in the amount of methane relative to hydrogen at low latitudes. Similar effects are seen for the 2002 observations. For μ=0.8 (Fig. 12B), which probes more deeply, the changes are even more dramatic. A color composite of these wavelengths (using R=930 nm, G= 834.6 nm, and B= 826.8 nm) is shown in Fig. 14, where the three components are balanced to produce comparable dynamic ranges for each wavelength. This results in nearly blue low latitudes where absorption at the two methane dominated wavelengths is relatively high and green/orange polar regions as a result of the decreased absorption by methane there.

[Figure 11 about here.]

[Figure 12 about here.]

[Figure 13 about here.]

The spectral comparisons in Figs. 12, 13, and 14 also reveal substantial secular changes between 2002 and 2012. At wavelengths for which methane and/or hydrogen absorption are important, the northern low-latitudes have brightened substantially, while the southern low latitudes have darkened. The 2002-2012 differences shown in Fig. 12 are not due to a view-angle effect because comparisons in that figure are made at the same view and illumination angles for both years. The bright bands between 38° and 58° (north and south) have also changed significantly, with the southern band darkening dramatically, while the northern band brightened by a smaller amount. The northern bright band in 2012 was of lower contrast than the southern bright band was in 2002. However, at continuum wavelengths

(Fig. 13) secular changes are not evident. Aside from what appears to be a 2% calibration disagreement between 2002 and 2012, the latitudinal variations are very similar for both epochs. [The 2002 calibration we use here is based on WFPC2 comparisons and leads to I/F values that are 3% smaller than published by KT2009.] This lack of continuum differences is partly a result of the relatively smaller impact of particulates at short wavelengths where Rayleigh scattering is more significant. At absorbing wavelengths the optical depth and vertical distribution of particulates have a greater fractional effect on I/F and thus small secular changes in these parameters can be more easily noticed.

[Figure 14 about here.]

5 A simplified model of methane/hydrogen variations

5.1 Model description

KT2009 estimated the latitude variation of the CH_4 volume mixing ratio using a simple model to fit the spectral region where hydrogen and methane have comparable effects on the observed I/F spectrum. They assumed that in the region from 819 nm to 835 nm the I/F spectrum would behave as a reflecting layer attenuated by methane and hydrogen in proportion to their relative absorption strengths, i.e.

$$I/F = \exp(C_0 + C_1 \times k_{CH_4} + C_2 \times k_{H_2}), \tag{2}$$

where k_{CH_4} and k_{H_2} are absorption coefficients of methane and hydrogen respectively. Because the methane coefficient is essentially independent of temperature and pressure, the coefficient C_1 is proportional to the amount of methane in the path above the cloud layer. But because k_{H_2} not only depends on temperature, but also on the square of the density, the corresponding claim cannot be made for C_2. In fact, the two absorption coefficients have different units, $(km - amagat)^{-1}$ for methane, and $(km - amagat^2)^{-1}$ for hydrogen, and the two gases also have different vertical distributions. However, if the pressure of the reflecting layer were independent of latitude, then these hydrogen dependencies

would not matter, and the variation in the ratio of C_1 relative to C_2 would be proportional to the variation of the methane/hydrogen mixing ratio (presuming the relative vertical distribution did not also vary). Our simplified model assumes that this relationship is true even if the aerosol distribution does vary somewhat, and is thus subject to an uncertain error. To evaluate the hydrogen absorption coefficient, KT2009 used an effective fixed temperature of 80 K, which we also used because it provided an approximate overall best fit to the spectra over a range of latitudes. We also followed KT2009 in assuming equilibrium hydrogen.

[Figure 15 about here.]

While KT2009 chose ten samples from 819 to 835 nm, we here use all 50 wavelengths in this range. In computing the χ^2 estimates of fit quality, we assumed a somewhat arbitrary value of 2% in relative I/F calibration-absorption modeling error and root-sum-squared that with the center-to-limb fitting errors. We used an arbitrary scaling of the k_{H_2} coefficients, then carried out a non-linear regression to obtain best fit model coefficients, uncertainties, and the ratio of C_1/C_2 and its uncertainty. Additional uncertainty is present due to physical flaws in the assumptions of the model. The sample fits provided in Fig. 15 show that the model is quite successful at fitting the observed spectra, and also allows tight constraints on the model coefficients and on the ratio of coefficients, which we use as a proxy for the CH_4 /H_2 ratio.

5.2 Model results for latitude dependence of CH_4/H_2.

Fitting this crude model to every latitude for both 2002 and 2012 center-to-limb fits leads to the latitude dependence shown in Fig. 16. Here we use a scaling that best matches the methane volume mixing ratio (VMR) values estimated from full radiation transfer modeling that properly accounts for the density dependence and temperature dependence of hydrogen absorption (discussed in subsequent sections). It is noteworthy that a single scale factor applied to all latitudes yields remarkable consistency with the full radiation transfer results at three different latitudes with different aerosol reflectivities. Using the same

scale factor on the 2002 profile leads to about a 4% overall average between 30° S and 20° N. There are substantial differences between 2002 and 2012 where the two profiles overlap, though many of the small scale variations occur at nearly the same latitudes. The relative variations between 35° S and 35° N have a correlation of 70%, with the 2012 variations being about 10% larger than the 2002 variation. Yet the average 2012 methane VMR is closer to 4.5% at low southern latitudes where the 2002 profile is closer to 3.8%. Some of this difference might be due to the difference in aerosol structure, which is indicated by the higher brightness of the southern hemisphere in 2002 (see Fig. 12). Most of the small scale variability seen in the 2002 ratio is due to the hydrogen absorption term. It is hard to understand how this could occur without any evident small scale variability in the aerosol term (Fig. 12B). It suggests small-scale temperature variations or vertical mixing variations that produce changes in para fractions. A significant part of the small scale structure seen in the 2012 methane VMR values is also due to hydrogen coefficient variations as well, especially north of 60° N where the model cloud reflectivity varies relatively smoothly with latitude (Fig. 16B), at least at these wavelengths (small variations are seen at near-IR wavelengths, as discussed later).

It should be noted that there are many options for simplified modeling of the methane to hydrogen ratio variations with latitude. Different zenith angle choices lead to somewhat different results; in fact using small μ values provides improved fit quality relative to larger values, but these samples don't reach as deeply into the atmosphere. It is also possible to make slightly more complicated models, fitting the effective temperature of hydrogen at each latitude, for example. When that is done under the assumption that the para fraction is at equilibrium, the temperature varies with latitude from about 75 K at high northern latitudes to about 90 K at high southern latitudes. In this case the temperature varies on a small scale, which may be responsible for the small scale variations of the hydrogen absorption term seen in the simpler model. It is also possible to fit both the effective temperature of CIA absorption and the para fraction. This allows for much improved fit quality at low latitudes, resulting in generally

higher effective temperatures, but higher para fractions that are more compatible with much lower temperatures. This could only be obtained by downward mixing of the higher stratospheric para fractions at all latitudes, which is not plausible. To obtain a best fit para fraction that is in thermal equilibrium, the effective temperature needs to be near 80 K. We decided to stick with the simpler model as a crude means of interpolating between latitudes where full radiation transfer models provide more reliable tie points.

[Figure 16 about here.]

Also noteworthy is the difference between 2012 north and 2002 south polar regions (there is no overlap between 2002 and 2012 in either polar region). In 2002 the mixing ratio from 75° S to 50° S is close to 2.4% and exhibits only small variations with latitude, while the 2012 profile at equivalent northern latitudes displays substantial and nearly sinusoidal variations with a latitudinal wavelength near 10°. It should be noted that each of these points is derived from 50 wavelengths and is thus far less noisy than one might suspect based on the plots of single wavelengths, as in Figs. 12 and 14. The reality of these high-latitude features is further supported by the fact that the same analysis applied to similar latitudes in the opposite hemisphere using 2002 observations did not find such large variations, suggesting that the variations are more likely due to a hemispheric difference rather than an inherent high latitude artifact of the analysis. Also, there is no obvious reason why such artifacts should suddenly disappear at latitudes below 60° N.

5.3 Comparison of high-latitude model results with Keck imaging.

Given the strong possibility that the high latitude variations in effective methane VMR are real, we looked for some evidence of a similar pattern in the high-resolution near-IR Keck images from 2012. These are much more sensitive to cloud structure due to use of longer wavelengths and higher spatial resolution (often reaching 0.06 arcseconds). Initially we suspected that latitude bands with more “con-

vective" cloud features might be correlated with regions of upwelling and thus increased methane VMR values. To test this idea we started with H-band Keck images from 16 August 2012 and 4 November 2012 (before and after our STIS observations). These were mosaicked to form a high signal-to-noise images using techniques described by Fry et al. (2012). These were high-pass filtered to enhance the contrast of faint cloud features, then zonally averaged over 90° in longitude to define any latitudinal pattern that might be present at high northern latitudes.

The comparison results are shown in Fig. 17. We found significant correlations between the zonal mean cloud variations and the zonal mean methane VMR variations over the 55° N to 82° N latitudinal range. But the correlation surprised us in being negative instead of positive. Correlation coefficients for the two sets of variations are -0.552 for 15 August (significant at the 0.14% level) and -0.513 (significant at the 0.29% level) for 4 November, or -0.683 (significant at the 0.036% level) for 4 November if STIS results are shifted 1° N (a similar shift for the 15 August results produces little change in the correlation coefficient). The significance levels quoted are the probabilities that normally distributed random variables could produce correlations this negative (or more negative), using statistics based on 10^7 trials. A possible physical interpretation of the anticorrelation is that where the effective methane amount is reduced, the cloud features become more visible due to reduced absorption above the clouds. The depth of these small high-latitude cloud features is roughly constrained by 2011 observations in H and Hcont filters, from which Sromovsky et al. (2012) found that most were deeper than the methane condensation level, many near 2 bars, under the assumption of no methane depletion and using the F1 structure and methane profile. If we account for the methane depletion at high latitudes, these pressure estimates would increase, and thus might be below the level of significant depletion.

It is also worth noting that the pattern of high-latitude cloud brightness variations in the Keck images north of 55° N is relatively stable over time, when averaged over longitude. Both 16 August and 4 November 2012 images show similar patterns in Fig. 17, with larger amplitudes present in the 4 Novem-

ber image, probably due to better seeing conditions on the night these images were acquired. We also found similar patterns in Keck/NIRC2 H-band images acquired on 25 July 2012 and 15 August 2013. While some details of the pattern do vary, the location of minima seem to be relatively unchanged over at least a year.

[Figure 17 about here.]

6 Full radiative transfer modeling of methane and aerosol distributions

The spectral profile comparisons (Figs. 10, 11, and 12), and especially the somewhat more quantitative modeling of Fig. 16, strongly suggest that there is a permanent and more or less symmetric high latitude methane depletion on Uranus. But, because hydrogen absorption has a density squared dependence, and the methane has a vertically varying mixing ratio, a more accurate constraint on methane requires full radiative transfer modeling, including the effects of more realistic aerosol distributions, as described in the following. The more complete modeling is also needed to provide the scaling factor that converts the C_1/C_2 ratio plotted in Fig. 16 to a methane VMR.

6.1 Radiation transfer calculations

We used the radiation transfer code described by Sromovsky (2005a), which include Raman scattering and polarization effects on outgoing intensity, though this is a minor virtue at the wavelengths employed in our analysis. To save computational time we employed the accurate polarization correction described by Sromovsky (2005b). After trial calculations to determine the effect of different quadrature schemes on the computed spectra, we selected 10 zenith angle quadrature points per hemisphere and 10 azimuth angles. Calculations with 14 quadrature points and 14 azimuth angles changed fit parameters by about 1%, which is much less than their uncertainties. To characterize methane absorption at CCD wavelengths we used the coefficients of KT2009. To model collision-induced opacity of H_2-H_2 and He-H_2

interactions, we interpolated tables of absorption coefficients as a function of pressure and temperature that were computed with a program provided by Alexandra Borysow (Borysow et al. 2000), and available at the Atmospheres Node of NASA'S Planetary Data System. We assumed equilibrium hydrogen for most calculations, following KT2009 and Sromovsky et al. (2011).

6.2 Cloud models

We initially used two different models of cloud structure for comparison purposes. The first is nearly identical to the model of KT2009, which we will refer to as the KT2009 model, and the second is a modified version of the KT2009 model, which we will refer to as the compact cloud layer model, or compact model, which is the same model used by Sromovsky et al. (2011). These models are compared in Fig. 18 and described in the following subsections. After trial fits to the STIS spectra we found that the compact model provide generally much better fits, due to its greater flexibility in how particles can be vertically distributed. Thus most of the fit results are based on compact model fits.

[Figure 18 about here.]

6.2.1 The KT2009 vertically diffuse model

As illustrated in Fig. 18A, this model has four layers of aerosols, the uppermost being a Mie-scattering stratospheric haze layer characterized by an optical depth at 0.9 μm, a gamma size distribution Hansen (1971), with a mean radius of a =0.1 μm and a normalized variance of b =0.3. These particles are assumed to have a real index of 1.4, and an imaginary index following the KT2009 relation

$$n_i(\lambda) = 0.055 \exp[(350-\lambda)/100], \tag{3}$$

for λ in nm and is only applicable between 350 nm and 1000 nm (as are the subsequent equations). This upper haze was distributed vertically above the 100 mb level with a constant optical depth per bar. The remaining layers in the KT2009 model are characterized by a wavelength-independent optical depth per

bar and a wavelength-dependent single-scattering albedo, given by

$$\varpi_t(\lambda) = 1 - 1/[2 + \exp[(\lambda - 290)/37]], \tag{4}$$

again for λ in nm. Their adopted double Henyey-Greenstein phase function for the tropospheric layers used g_1 =0.7, g_2=-0.3, and a wavelength-dependent fraction for the first term, given by

$$f_1(\lambda) = 0.94 - 0.47 \sin^4[(1000 - \lambda)/445], \tag{5}$$

which produces a backscatter that decreases with wavelength, as shown in Fig. 19. The three tropospheric layers are uniformly mixed with gas molecules, with different optical depths per bar in three distinct layers: 0.1-1.2 bars (upper troposphere), 1.2-2 bars (middle troposphere), and P>2 bars (lower troposphere). These optical depths per bar parameters are the adjustable ones we use to fit this model to the observations.

[Figure 19 about here.]

6.2.2 The compact cloud layer model

This model is a modification of the KT2009 diffuse model. As illustrated in Fig. 18B and summarized in Table 3, the main change we made was to replace the KT2009 middle tropospheric layer with two compact layers: an upper middle tropospheric cloud layer (UMTC) and a lower middle tropospheric cloud layer (LMTC). The UMTC layer is composed of Mie particles, which we characterized by a gamma size distribution with an adjustable mean particle radius and a fixed normalized variance of 0.1, a fixed refractive index of 1.4, and an imaginary index of zero. The particle radius was initially fixed at 1.2 μm, following our analysis of the 2002 observations because the radius did not vary much from that value in preliminary fits. But in the current analysis smaller values between 0.2 μm and 0.6 μm were preferred. This probably results from the changed calibration, which produces a greater darkening with increasing wavelength. This favors smaller particles, which provide a greater decline in backscatter

efficiency with wavelength (Fig. 20). For the LMTC layer we used particles with the same scattering properties as given by KT2009 for their tropospheric particles. Both of these compact layers have the bottom pressure as a free (adjustable) parameter and a top pressure that is a fixed fraction of 0.93 $\times$ the bottom pressure. This degree of confinement is approximately the same as obtained for the cloud layer inferred from the occultation analysis (Sromovsky et al. 2011). The motivation for introducing these replacement layers was to obtain more flexibility in vertical structure and to allow the possibility of including a thin cloud near the methane condensation level, as suggested by the occultation analysis of Sromovsky et al. (2011).

[Figure 20 about here.]

[Table 3 about here.]

The last change we made was to replace the KT2009 bottom tropospheric layer by a compact cloud layer at 5 bars (the BTC, or bottom tropospheric cloud), with adjustable optical depth and with the KT2009 tropospheric scattering properties. Sromovsky et al. (2011) found that this layer was needed to provide accurate fits near 0.56 and 0.59 μm, but its pressure was not well constrained by the observations (pressure changes could be compensated by optical depth changes, to produce essentially the same fit quality). Whether this deep cloud is vertically diffuse or compact also could not be well constrained.

The wavelength dependence of the extinction efficiency, asymmetry parameter, backscatter phase function, and backscatter efficiency, are given in Fig. 20 for the range of Mie particles we considered for the putative methane layer (the UMTC layer). We also show corresponding values for the KT2009 tropospheric particles, where applicable. The KT2009 tropospheric particles have wavelength independent optical depth, and thus the way its backscatter efficiency varies with wavelength is entirely determined by the phase function (defined by Eq. 5). For all the Mie particle sizes shown, there is a decline in backscatter efficiency with wavelength, but not as large as for the KT2009 tropospheric particles. For

optically thin particle layers, the reflectivity of the layer is largely determined by the backscatter efficiency. For optically thick layers other aspects of the phase function are also important.

6.2.3 Other cloud models

Tice et al. (2013) found that two cloud layers were needed to fit IRTF spectra of Uranus from 0.8 to 1.8 μm. Each cloud layer has three retrieved parameters: total optical depth, cloud base pressure, and fractional scale height. Their tropospheric cloud model assumed that the scattering cross section varied with wavelength as if the particles were perfect spheres of $\sim$1 μm in radius and with a refractive index of 1.4+0i. But the phase functions were assumed to be of Henyey-Greenstein form, with $g = 0.7$. In addition, a wavelength dependent single-scattering albedo was added, using ϖ=1.0 for $\lambda < 1$ μm, decreasing to ϖ=0.7 between 1 and 1.4 μm, and keeping ϖ at 0.7 for $\lambda > 1.4$ μm. This cloud is optically thick, but vertically thin, located between 2 and 3 bars. This pressure estimate is related to their assumed 1.6% deep methane VMR. Their best fit for the particle radius was 1.35 μm, but this is suspect because they did not allow for any wavelength dependence in the particle phase function, and the tacked-on single-scattering albedo would also influence the derived radius.

To improve the fits shortward of 1.2 μm, they added an optically thin haze layer of different kinds of particles at pressures below 1 bar. These particles had a best fit radius of 0.1 μm, used to obtain the (initial) wavelength dependence of the scattering cross section. Such small particles would be expected to be fairly isotropic scatterers, but Tice et al. (2013) again assumed H-G phase functions with $g = 0.7$. They also added a strong wavelength dependent single scattering albedo, which dropped from 1 at 0.8 μm to 0.6 at 1 μm then back up to 1 at 1.1μm. These strong variations in single-scattering albedo were not needed in our haze models. Tice et al. (2013) used for most of their analysis a deep methane VMR of 1.6% but limited to a 30% relative humidity “at all levels” (sic). Presumably they also capped the mixing ratio in the stratosphere, though they did not include that information in their paper. Such a profile is not consistent with the Voyager occultation results of Lindal et al. (1987), which require

that the above-cloud methane humidity be 0% for deep methane volume mixing ratios of 1.8% or less. Another inconsistency is that they used a temperature structure matched to the Lindal et al. model D profile, which is only consistent with the occultation measurements for a deep methane mixing ratio of 2.23%. These temperatures are too high for their assumed methane mixing ratio, which changes the shape of the hydrogen absorption feature (reducing its spectral amplitude) from what it would be with a consistent profile.

6.3 Fitting procedures

To avoid the complexity of fitting a wavelength-dependent imaginary index in the methane layer (the UMTC layer in Table 3) we fit only the wavelength range from 0.55 μm to 1.0 μm. We chose a wavenumber step of 118.86 cm^{-1} for sampling the observed and calculated spectrum. This yielded 69 spectral samples, each at three different zenith angle cosines (0.3, 0.4, and 0.6), for a total of 207 points of comparison. Our compact layer model has seven or eight adjustable parameters (see Table 3), leaving 192 or 193 degrees of freedom. We fixed the BTC base pressure to 5 bars (see Table 3). While Sromovsky et al. (2011) fixed the UMTC mean particle radius at 1.2 μm, we kept this adjustable and were surprised to find that a much smaller radius was preferred, ranging from 0.15-0.6 microns. This is very likely due to the revised albedo calibration function (Fig. 4), which produces a stronger I/F decline with wavelength that is better matched by smaller particles (see Fig. 20). To fit the KT2009 model we followed their approach by adjusting only the four $d\tau/dP$ (optical depth per bar) values We used a modified Levenberg-Marquardt non-linear fitting algorithm (Sromovsky and Fry 2010) to adjust the fitted parameters to minimize χ^2 and to estimate uncertainties in the fitted parameters. Evaluation of χ^2 requires an estimate of the expected difference between a model and the observations due to the uncertainties in both. We followed the same approach for estimating uncertainties as used by Sromovsky et al. (2011). The uncertainty in χ^2 is expected to be $\sim$25, and thus fit differences within this range are not of significantly different quality.

7 Compact model fits

The compact model described previously provides provides generally better fits than the diffuse models, reaching χ^2 values in the mid 200's compared to mid 300's to low 500's for the diffuse model. This is presumably due to its greater flexibility to fit vertical distributions because the main cloud layer is divided into two sublayers with adjustable pressures as well as adjustable optical depths. Another difference from diffuse models is that its upper sublayer has wavelength dependencies controlled by Mie scattering, which is parameterized by particle radius and refractive index, rather than the wavelength-dependent double Henyey-Greenstein parameters of of the lower sublayer, which we take to be those of KT2009, as given by Eqs. 4 and 5.

We first constrain the effective methane mixing ratio profile at key latitudes to define the scaling factor for Fig. 16, then try to fit the best-fit equatorial profile over a wide range of latitudes to discover where it does not apply. At latitudes north of 30°we obtain improved fits by reducing the effective mixing ratio. But the best fits are obtained with a depletion profile that exhibits decreasing depletion with increasing depth, which also is more physically plausible than a uniform depletion at all depths.

7.1 Constraining equivalent methane mixing ratios at key latitudes

The detailed latitudinal variation of the equivalent methane mixing ratios plotted in Fig. 16 is based on a scaled ratio of fit coefficients (C_1/C_2). To define that scaling, we used fits that fully account for the different vertical absorption profiles of hydrogen CIA and methane, carried out at three latitudes covering the range of mixing ratio variation (10° S, 0°, and 60° N). To estimate the optimum equivalent deep methane mixing ratio at each latitude we did compact model fits for a variety of methane profiles (D1, DE, E1, EF, F1, FG, and G) that have a range of deep methane mixing ratios (2.22%, 2.76%, 3.20%, 3.6%, 4.00%, 4.5%, and 4.88%, respectively). These profiles are all consistent with the Voyager 2 occultation measurements of Lindal et al. (1987), and thus also have different temperature and above-

cloud methane profiles. They are all from Sromovsky et al. (2011) except for DE and FG, which were also constructed to be occultation consistent using the same techniques as Sromovsky et al. (2011). The fit results at our selected key latitudes are plotted in Fig. 21, where we show two fit quality measures as a function of the deep methane mixing ratio of the profiles that were employed. The two measures are χ^2 and the error at 825 nm divided by the error expected just from measurement errors. At two latitudes the minimum χ^2 occurs at a lower methane mixing ratio than the minimum error at 825 nm: 4% vs 4.6% at 10° S, 3.2% vs 3.8% at the equator. This might also have been true at 60° N, had we tried profiles with lower deep mixing ratios. The diffuse model fits at the equator yielded the same mixing ratio estimates as the compact model, but χ^2 values were significantly higher. We consider the 825-nm estimate to be the most relevant since it provides the most direct comparison between methane and hydrogen absorptions and uses the μ = 0.6 spectrum to weight the deep atmosphere more than the overall fit, which uses μ = 0.3, 0.4, and 0.6. The 825-nm comparison thus provides the most direct constraint on the methane mixing ratio, which leads to estimates of 4.6±0.5% at 10° S, 3.8±0.5% at the equator, and 1.9±0.5% at 60° N. These points were plotted in Fig. 16 as filled circles. It is slightly surprising how these results lead to such a consistent scaling for the simplified model. The average is sufficiently close to the F1 profile value of 4% that we used F1 as our base profile for low latitudes.

Note that an occultation consistent profile with a deep mixing ratio as low as 1.6%, which is the deep VMR assumed by Tice et al. (2013), would be grossly inconsistent with the observed spectra at low latitudes. Though Tice et al. (2013) were able to fit their spectra with such low methane VMR values, they may have been able to make up for lacking methane absorption at longer wavelengths by assuming low single-scattering albedos in their main cloud layer. Also, based on sample spectral fits shown in their Figs. 4, 7, and 15, they did not fit very well the critical spectral region near 825 nm, where their model spectra show relatively more hydrogen absorption than the observations, which indicates that their methane mixing ratio is too low. They also reduce the weight of this spectral region

in their fits by assigning relatively large uncertainties compared to other regions with similar I/F values. Their fits were also aided by using much more above-cloud methane than would be allowed by the 0% relative humidity allowed by the Voyager 2 occultation results of Lindal et al. (1987) for their assumed deep mixing ratio.

[Figure 21 about here.]

7.2 Compact model fits versus latitude for the F1 profile

We first tried to fit the compact model to a range of latitudes, while assuming that the F1 profile of temperature and methane applied to all latitudes. The entire set of results is plotted in Fig. 22, and results for latitudes up to 30° N are presented in Table 4. There are several remarkable features of these fits. First, the $m1$ vertically diffuse stratospheric haze layer is found to have negligible opacity north of 25° N. Whether this is a real effect and a real change from the structure inferred from 2002 observations or a result of a different spectral calibration using WFC3 observations is not clear at this moment. Perhaps a related difference is that the upper sublayer (UMTC) of the main cloud layer, a Mie layer, has a fitted particle radius that is just a fraction of a micron, much smaller than the values inferred from our analysis of 2002 STIS observations. This might also be affected by a calibration change.

[Table 4 about here.]

At the equator the results are also unusual. In diffuse model fits we found that the upper tropospheric haze provided a sharply increased contribution at the equator, and seems to be the main change associated with the bright equatorial band visible in many images at wavelengths of intermediate methane absorption (e.g. Fig. 3K, and S). In the compact model fits, however, changes in the lower and higher layers seem to be relatively more important, with changes in $m2\_p$ and $m2\_r$ as well as $m1\_odpb$, playing a role. The derived value of $hg1\_odpb$ for the compact model is comparable to its uncertainty and was ignored for most compact model fits.

Between perhaps 30° S and 50° N, the fit quality is seen to be relatively flat, with the exception of substantial dips in χ^2at the equator and near 30° N. The 825-nm signed error, given by (model-observed)/uncertainty, is also relatively flat over the same latitude range. The small positive error seen in this at most latitudes in this range suggests that the mixing ratio in the F1 profile is not quite large enough. The rather large negative 825-nm errors found at high latitudes are associated with excessively high methane mixing ratios in the model calculations.

[Figure 22 about here.]

Beyond 40° N, the 825-nm signed error becomes much larger as the overall fit quality measured by χ^2 becomes much worse. This indicates that the assumed latitude-independent profile of methane is not consistent with the observations. A different methane profile is clearly needed at high latitudes as was already demonstrated at 60° N from fits used to define the scaling of the simplified model.

7.3 The need for shallow methane depletion

While structure and methane profiles with a 2% CH_4 deep mixing ratio provide the best fits at 60° N compared to other profiles with constant mixing ratios up to the condensation level, the deep contrast between equator and pole (2% VMR to 4% VMR) is not physically plausible. Such deep latitudinal gradients in composition would lead to density gradients along isobars. As a consequence of geostrophic and hydrostatic balance, these gradients would lead to vertical wind shears (Sun et al. 1991). These vertical wind shears acting over the entire atmosphere would likely lead to cloud top winds that would be highly incompatible with the observed winds. Thus we considered methane vertical distributions in which the higher latitudes had depressed mixing ratios restricted to shallow depths in the upper troposphere only. As indicated by KT2009, the 2002 spectral observations did not require that methane depletions extend to great depths, and Sromovsky et al. (2011) showed that shallow depletions were preferred by the 2002 spectra. We will show here that the 2012 spectral constraints also favor relatively

shallow methane depletions.

Here we constructed profiles with shallow CH_4 depletion using the "proportionally descended gas" profiles of (Sromovsky et al. 2011) in which the model F1 mixing ratio profile $\alpha(P)$ is dropped down to increased pressure levels $P'(\alpha)$ using the equation

$$P' = P \times [1 + (\alpha(P)/\alpha_d)^{vx}(P_d/P_c - 1)] \quad \text{for} \quad P_{tr} < P < P_d, \tag{6}$$

where P_d is the pressure depth at which the revised mixing ratio $\alpha'(P) = \alpha(P')$ equals the uniform deep mixing ratio α_d, P_c is the methane condensation pressure before methane depletion, P_{tr} is the tropopause pressure (100 mb), and the exponent *vx* controls the shape of the profile between 100 mb and P_d. Profiles of this type are shown in Fig. 23. The profiles with $vx = 1$ are similar in form to those adopted by Karkoschka and Tomasko (2011). Smaller values of *vx* produce more rapid declines of methane VMR above the P_d level (as pressure decreases).

[Figure 23 about here.]

7.4 Compact model fits at 60° N vs depletion depth

It is clear that a lower methane mixing ratio is required at high latitudes, but it is not reasonable to expect that lower ratio to extend to great depths because that would require a large horizontal wind difference between low and high latitudes, as noted previously. It is also necessary to find a sink of methane that can deplete methane locally in the troposphere. The only one we know of is methane condensation, which can cause the stratosphere to be dry (sub saturation methane mixing ratios) and, when mixed downward, can cause local depressions of the methane mixing ratio in the upper troposphere. Thus we expect only the upper troposphere to be depleted and the question is whether we can constrain the depth of that depression using STIS observations.

Here we start with an F1 profile at 60° N and then deplete the methane above a base pressure P_d using Eqn. 6 and controlled by the secondary parameter *vx*, which causes rapid depletion with decreasing

pressure when set to small values and smaller depletion rates when set to larger values. Sromovsky et al. (2011) found that $vx = 1$ seemed to be preferred by the 2002 data set, but we found larger values preferred by the 2012 data set (this might also be true for 2002 if explored more extensively and with the 2012 calibration function). We tried a range of P_d values for vx ranging from 0.5 to 5. Subsets of our results are plotted in Fig. 24, which displays χ^2 and 825-nm error values as a function of P_d for different assumed values of vx. The optimum values are summarized in Table 5. We found that χ^2 minima appear at increasing depths as the depletions become more gradual with decreasing pressure (for larger values of vx). The best fit at 60° N was found for $vx = 3.0$, with $P_d = 30$ bars to minimize χ^2 and 16 bars to minimize the 825-nm error. The χ^2 minimum is near 10 bars for $vx = 2$ and somewhat larger than the minimum for $vx = 3$, while the minimum 825-nm error is found at 7.5 bars, closer to the χ^2 minimum than for the $vx = 3$ case. Clearly, $vx = 1$ is a very poor choice. But even that profile fits better (χ^2 = 333) than the D1 profile (χ^2 = 359), which is the best fitting of the occultation consistent profiles with vertically uniform mixing ratios. The vertical variation of methane VMR for the best fit P_d value is shown for each vx case in Fig. 25A. Note that shallower and deeper depletions all produce similar mixing ratios near 1.7 bars, and that greater depletions at depth result in somewhat higher mixing ratios at pressures below 1.7 bars. It might be worthwhile to explore other depletion functions with different vertical variations.

[Figure 24 about here.]

7.5 Latitudinal variation in depletion depth and aerosol structure

To fix the problem of poor spectral fits at latitudes beyond 30° N, we chose a $vx = 2.0$ vertical variation function and found the best-fit value of P_d as a function of latitude. The χ^2 and 825-nm error results as a function of P_d are plotted in Fig. 26. Best-fit values for these parameters are presented in Table 5 and the best-fit aerosol parameters in Table 4. The best-fit results are also plotted in Fig. 22 (right panels) for

comparison with the fits using the undepleted F1 profile at all latitudes. The depletion depth increases from 30° N to 70° N (the highest latitude fit) and in this region χ^2 and 825-nm errors have been greatly reduced relative to the prior fits with undepleted profiles.

[Figure 25 about here.]

[Figure 26 about here.]

One puzzling result is that the cloud layer that we thought was associated with methane condensation (the *m*2 or UMTC layer) continues into the polar regions where methane condensation should not occur because of the decreased methane mixing ratio. Perhaps we should not have used the same labels for *m*2 points at high latitudes that we used at latitudes from 30° S to 30° N (see right panel of Fig. 22). In fact, the sharp drop in optical depth of the *m*2 layer between 20° N and 30° N might have continued northward, and what we identified as the *m*2 layer north of 30°, might actually be a continuation of the *hg*2 cloud. In that case, the layer we identified as the *hg*2 cloud in these northern fits might actually have a different composition from the corresponding layer at low latitudes. Also note that the *hg*3 layer declines dramatically north of 50° N, where *Pd* exceeds the assumed depth of the cloud layer. The polar region possibly has a completely new set of cloud layers.

[Table 5 about here.]

7.6 Layer contributions and comparison of modeled to measured spectra

The relative roles played by each of the significant model layers in creating the observed spectral characteristics and the effect of the *m*2 layer particle size, are illustrated in Fig. 27B-F. The model shown is an undepleted F1 profile at the equator. The contribution of the *hg*1 layer is insignificant, and therefore not shown. In the difference spectra for different parameters we see different spectral shapes and different responses to view angle changes. This is what makes it possible to constrain the parameters in the fitting

process. Recall that the fits are done only over the 550 nm to 1000 nm spectral range, while these comparisons extend to 300 nm. In panel A, we show how the fit compares to the observed spectrum. Even below the wavelength range of the fit, the model and measured spectra are generally within 10% of each other, a difference that could be significantly reduced by modifying the single-scattering albedo function below 550 nm. Also note that the larger fractional errors in this comparison are at wavelengths where noise levels are substantial. This is more readily seen in Fig. 28, where spectral ratios are compared with expected uncertainties.

[Figure 27 about here.]

[Figure 28 about here.]

8 Discussion: Methane as a constraint on meridional motions.

The inferred methane depletion at high latitudes requires a sink for methane, which we take to be methane condensation, the only sink identified below the stratosphere. Below the methane condensation level, decreasing the methane mixing ratio requires mixing in (or descent) of methane depleted gas, the only source of which exists above the methane condensation level. Fig. 29 illustrates a plausible mechanism. Rising methane-rich gas at low latitudes is dried out by condensation and sedimentation of methane ice particles. That dried gas is then transported to high latitudes, where it begins to descend, bringing down methane depleted gas, which then gets mixed with methane-rich gas on its return flow. Without lateral eddy mixing across the streamlines, the only restoration of the methane mixing ratio would be through evaporation of the precipitating condensed methane at low latitudes. The depth of the depletion at high latitudes might be controlled by the depth of the meridional cell or the depth at which cross-streamline mixing predominates. The suggested circulation would promote formation of optically thin methane clouds (or hazes) at low latitudes, but inhibit methane cloud formation at high latitudes. This seems consistent with the lack of observed discrete cloud features south of 45° S. However, we

have seen discrete cloud features at high northern latitudes (Sromovsky et al. 2009), which might very well be composed of something other than methane, given that their cloud tops seem to be deeper than the methane condensation level (Sromovsky et al. 2012). The general downwelling would also tend to inhibit all condensation clouds, as sub-condensation mixing ratios would be created by such motions. However, this does not rule out localized regions of upwelling and formation of condensation clouds occupying a small fractional area.

[Figure 29 about here.]

The circulation cell in Fig. 29 would need to be very deep to be consistent with microwave observations probing the 10-100 bar region of Uranus (Hofstadter et al. 2007). These reveal a symmetry pattern in which microwave absorbers (NH_3, H_2S) are depleted at both high southern and high northern latitudes, suggesting a non-seasonal equator-to-pole meridional circulation, with upwelling at low latitudes and down-welling at high latitudes (de Pater and Lissauer 2010), similar to the northern circulation cell illustrated in Fig. 29. If this deep cell extended to the upper troposphere, it could be consistent with a shallow CH_4 depletion, as long as the flow at the 2-3 bar level was dominated by poleward flow that did not go through the drying-by-condensation process, as suggested by the inner streamline in the southern flow pattern in Fig. 29. While our best fits indicate that the largest fractional depletions occur in the upper troposphere, at higher latitudes some degree of depletion could extend deeper than the 10-bar level. Because these deep meridional cells would likely be dominated by deep atmospheric conditions, they would probably have the same symmetry properties as the deep atmosphere (symmetry about the equator), which would suggest qualitatively that the north and south polar regions should not look very different.

However, a single deep cell in each hemisphere would provide a meridional flow that would oppose the observed equatorward motion of the long-lived and largest discrete cloud feature seen on Uranus, known as the Berg (Sromovsky and Fry 2005; Sromovsky et al. 2009). Its motion is more compatible

with a shallow depth for the upper tropospheric meridional cell, in which case the deep and upper tropospheric circulations would need to be separated by a third cell. Such a cell could also be compatible with cloud formation at the H_2S condensation level. A possible cell configuration of this type is shown in Fig. 30, in which the deep cell produces high-latitude ammonia depletion through formation of an NH_4SH cloud at low latitudes, an intermediate cell produces high latitude condensation of H_2S, and the top cell provides high-latitude depletion of methane. A problem with a single deep cell is that it would seem to inhibit formation of H_2S condensation clouds that are good candidates for producing the bright bands that form between 38° and 58° in both hemispheres. In fact, such a simple circulation would tend to inhibit all condensation clouds at high latitudes, in spite of the fact that cloud particles of some kind are detected there. The three-layer cell structure offers more possibilities for widespread condensation clouds, but the resemblance between the speculated structure in Fig. 30 and the structure shown in the right panels of Fig. 22 is crude at best. While there seems to be a change in cloud structure between high and low latitudes, if the interpretation is restricted to models with condensation clouds only, it is hard to explain the existence of what seems to be an H_2S cloud at low latitudes where the three-layer cell structure would inhibit such a cloud.

[Figure 30 about here.]

On the other hand, the drift of the Berg may not be a relevant constraint on meridional flow. If the cloud features comprising the Berg were generated by an unseen vortex, its drift may be controlled more by the vorticity of the zonal flow than by weak meridional flows (Lebeau and Dowling 1998). In addition, Hadley cell configurations with hemispherical symmetry are not consistent with recent numerical modeling of the seasonal circulation of Uranus by Sussman et al. (2012), which indicates that there should be tropospheric cross-equatorial flow peaking near equinox. Another point worth noting is that the presumed upwelling at low latitudes, which is supported by the inference of an optically thin methane cloud in those regions, is not accompanied by an abundance of discrete cloud features at those

latitudes. Likewise, the observed cloud structure at high northern latitudes, which appear somewhat deeper than expected for condensed methane, may be more related to localized upwellings rather than any broadly defined meridional cells. This may be similar to the situation on Jupiter in which a region of overall downwelling (a belt) contains many examples of localized convection and lightning (Showman and de Pater 2005). It is also conceivable that local increases in methane humidity might affect aerosol opacity even though the methane mixing ratio remained below saturation. The effect of water vapor humidity on the size and scattering properties of hygroscopic aerosols is significant and well known in the earth's atmosphere (Pilat and Charlson 1966; Kasten 1969). It is conceivable that a haze of hydrocarbon aerosols originally formed in the stratosphere might have their scattering properties altered in regions of varying methane humidity, even without the occurrence of methane condensation. Such an effect might even give the appearance of a condensation cloud in regions of local upwelling. However, we do not know if the background aerosols on Uranus would interact with methane in the same way as hygroscopic aerosols interact with water vapor in the earth's atmosphere.

Neptune also has a depletion of methane at high latitudes. Using 2003 STIS spectra of Neptune Karkoschka and Tomasko (2011) showed that between 80° S and 20° N the variation in Neptune's effective methane mixing ratio was very similar to that observed for Uranus. To explain this distribution they also suggested an upwelling at low latitudes, removal of methane by condensation, and downwelling of methane-depleted gas at higher latitudes to a depth of several bars. In this case the most active regions of cloud formation turn out to be in regions that should be downwelling to explain the methane depletion results. Thus, Neptune presents another example of cloud formation in regions of inferred downwelling. However, a recent paper by de Pater et al. (2014) suggests a very different meridional circulation for Neptune. Based on a multiwavelength analysis that included near-IR to microwave observations they detected warm polar and equatorial regions, where they infer downwelling motion, and cooler middle latitudes, where they infer upwelling motion. Such a circulation pattern is inferred to

extend to great depths and would seem to be in conflict with the pattern needed to produce the observed upper tropospheric methane depletion. Both planets seem to have more complicated stories than we are currently able to explain with simplified models.

9 Summary and Conclusions

We observed Uranus with the HST/STIS instrument in 2012, aligning the instrument's slit parallel to the spin axis of Uranus and stepping the slit across the face of Uranus from the limb to the center of the planet, building up half an image with each of 1800 wavelengths from 300.4 to 1020 nm. The main purpose was to constrain the distribution of methane in the atmosphere of Uranus, taking advantage of the wavelength region near 825 nm where where the hydrogen absorption competes with methane absorption and displays a clear spectral signature. Our analysis of STIS observations of Uranus from 2012 and comparisons with similar 2002 observations, as well as analysis of imaging observations from 2007, have led us to the following conclusions.

1. Final STIS 2012 albedo calibration corrections using WFC3 HST images from 2012 produces a larger decline of I/F with wavelength than was obtained from 2002 HST images. The FQ937N WFC3 image appears to be about 15% darker than would be consistent with the trend established by other filters.

2. Secular change at continuum wavelengths appears to be very small. When the KT2009 calibration is adjusted by 3% to match WFPC2 bandpass filtered images, the 2002 I/F value are found to be 2% greater than corresponding 2012 values. This is residual difference may be due to calibration uncertainties. The comparisons at wavelengths with noticeable gas absorption show that the northern hemisphere has brightened considerably since 2002, by about 25% at mid latitudes at 827 nm, and the southern hemisphere has darkened, by about 25% at mid latitudes at 827 nm.

3. In 2012 the methane mixing ratio in the upper troposphere of Uranus was depleted at high northern latitudes (relative to equatorial values), especially beyond 40° latitude, to a degree very similar to what was inferred for southern high latitudes from 2002 STIS observations. This is based on direct spectral comparisons of STIS latitudinal profiles at wavelengths with similar penetration depths but different amounts of hydrogen absorption.

4. We also found that the north and south depletions were simultaneous, as also suggested by the Tice et al. (2013) analysis of 2009 SpeX central meridian spectra, and thus probably not a seasonal effect. This is based on direct spectral comparisons near the 2007 equinox, using an HST/NICMOS F108N image that is sensitive to H_2 absorption and a Keck/NIRC2 PaBeta-filtered image that senses about the same atmospheric level, but is dominated by methane absorption. While both north and south high latitude regions have nearly equal brightness at these two wavelengths, at low latitudes the brightness of the F108N image exceeds that of the PaBeta image, indicating an increase in methane absorption and in the methane mixing ratio at low latitudes, at least in the upper troposphere.

5. We followed KT2009 in using a simplified model of the 815 nm - 835 nm spectral region to estimate the relative latitudinal variation of the methane volume mixing ratio. When this relative variation was absolutely scaled to match effective mixing ratios determined by full radiative transfer modeling at 10° S, the equator, and 60° N, we found that the effective mixing ratio varied on both large and small spatial scales. At the large scale we found the VMR to increase from roughly 2% within 30-40° of the poles to about 4-4.5% within 20-30° of the equator. The 2012 observations suggest an overall increase in methane VMR at low latitudes by about 0.5% relative to 2002.

6. The simplified model revealed a variation of $\pm$0.5% in methane VMR between 60° N and 82° N,

with a nearly sinusoidal variation with a period of about 10° in latitude. Similar variation was not seen in south polar regions using the same analysis techniques on a similar STIS data set from 2002.

7. Using Keck2/NIRC2 high-pass filtered H-band images from 16 August and 4 November 2012, we computed zonal averages and compared their variations with latitude with the methane VMR variations between 55° N and 82° N. We found similar patterns in August and November images and both had significant negative correlations with the methane VMR at significance levels of 0.14% to 0.29%. The explanation might be that latitude bands of reduced above-cloud methane makes the clouds appear brighter due to reduced methane absorption.

8. At the equator, the best fit, among vertical profiles with uniform deep mixing ratios and the occultation-consistent structure given by Sromovsky et al. (2011), is obtained with a mixing ratio near 4%, which matches the deep mixing ratio of their F1 profile.

9. Latitudinally scaled F1 profiles, accounting for gravity variations with latitude and assuming no temperature variation along isobars, lead to excellent fits not only at the equator, but from 30° S to 30° N for compact cloud models, but poor fits at high latitudes due to excessive methane absorption for this profile, indicating high latitudes are depleted in methane.

10. At high northern latitudes the best fit among vertical profiles with uniform mixing ratios up to the methane condensation level is obtained with a mixing ratio near 2%, although that low mixing ratio cannot plausibly extend to great depths because it would lead to problematic vertical wind shears.

11. At 60° N, we tried a variety of vertical variation functions for the methane depletion profile, characterized by the exponent *vx*, which we varied from 0.5 to 3.0. We found that the depletion depth P_d increased as the sharpness of the depletion decreased, with best-fit mixing ratios near

1.7 bars being comparable. The best fit was obtained for vx = 3, with vx = 2 providing a good with with somewhat better agreement between P_d that minimized χ^2 (10 bars) and the P_d that minimized the 825-nm error (7.5 bars).

12. We carried out fits to determine depletion depth as a function of latitude, assuming a profile shape defined by $vx = 2$. We found that P_d increased with latitude, beginning just beyond 30° N. At high latitudes the depth of the downwelling flow could exceed ten bars or more, although we are only sensitive to the upper tropospheric depletions, so that the depth may be partly a result of the particular empirical function we used in our models. Other profile shapes might be able to fit the data without producing as great a depth of depletion.

13. Using the depleted profiles to constrain the aerosol parameters, we found a downshift in the altitude (increase in base pressure) of the $m2$ layer north of 30° N. Since the lowered methane mixing ratio also implies that this layer can no longer be associated with widespread methane condensation (at lower latitudes it is located at the methane condensation level), it might here be composed of other materials or produced by widely dispersed local convective events, or produced by changes in background aerosols due to absorption of methane instead of condensation of methane.

14. The association of high-latitude methane depletions with descending motions of an equator-to-pole deep Hadley cell does not seem to be consistent with the behavior of the detected aerosol layers, at least if one ignores other cloud generation mechanisms such as sparse local convection. Both on Uranus and Neptune, aerosol layers seem to form in what are thought to be downwelling regions. A three-layer set of circulation cells offers some advantages in producing condensation clouds, but also fails to provide a good match to the detected aerosol layers.

In the future, better constraints on the vertical profile of methane as a function of latitude could be addressed by additional modeling work with the 2012 STIS spectra, trying different functional forms for vertical depletion profiles. Additional quantitative constraints might also be derived from analysis of the vertical wind shears that are implied by the horizontal density gradients associated with latitudinal compositional gradients. Additional work with numerical circulation modeling might also be productive in understanding how the methane mixing ratio affects and is affected by atmospheric circulation patterns.

Acknowledgments

This research was supported primarily by grants from the Space Telescope Science Institute, managed by AURA. GO-12894.01-A supported LAS and PMF. Partial support was provided by NASA Planetary Astronomy Grant NNX13AH65G (LAS and PMF). EK, HBH, IdP, and KAR also acknowledge support from STScI grants under GO-12894. We thank staff at the W. M. Keck Observatory, which is made possible by the generous financial support of the W. M. Keck Foundation. We thank those of Hawaiian ancestry on whose sacred mountain we are privileged to be guests. Without their generous hospitality none of our groundbased observations would have been possible.

References

Acton, C. H., 1996. Ancillary data services of NASA's Navigation and Ancillary Information Facility. Planet. and Space Sci. 44, 65–70.

Borysow, A., Borysow, J., Fu, Y., 2000. Semi-empirical model of collision-induced absorption spectra of H_2-H_2 complexes in the second overtone band of hydrogen at temperatures from 50 to 500 K. Icarus 145, 601–608.

Bostroem, K. A., Proffitt, C., 2011. STIS Data Handbook v. 6.0.

Colina, L., Bohlin, R. C., Castelli, F., 1996. The 0.12-2.5 micron Absolute Flux Distribution of the Sun for Comparison With Solar Analog Stars. Astron. J. 112, 307–315.

de Pater, I., Fletcher, L. N., Luszcz-Cook, S., DeBoer, D., Butler, B., Hammel, H. B., Sitko, M. L., Orton, G. O., Marcus, P. S., 2014. Neptune's global circulation deduced from multi-wavelength observations. Icarus 000, submitted.

de Pater, I., Lissauer, J. L., 2010. Planetary Sciences, 2nd ed. Cambridge University Press.

French, R. G., Elliot, J. L., Levine, S. E., 1986. Structure of the Uranian rings. II - Ring orbits and widths. Icarus 67, 134–163.

Fry, P. M., Sromovsky, L. A., de Pater, I., Hammel, H. B., Rages, K. A., 2012. Detection and Tracking of Subtle Cloud Features on Uranus. Astron. J. 143, 150–161.

Hansen, J. E., 1971. Circular polarization of sunlight reflected by clouds. Journal of Atmospheric Sciences 28, 1515–1516.

Hernandez, S., Aloisi, A., Bohlin, R., Bostroem, A., Diaz, R., Dixon, V., Ely, J., Goudfrooij, P., Hodge, P., Lennon, D., Long, C., Niemi, S., Osten, R., Proffitt, C., Walborn, N., Wheeler, T., York, B., Zheng, W., 2012. STIS Instrument Handbook, Version 12.0, (Baltimore: STScI). Space Telescope Science Institute, Baltimore, Maryland.

Hofstadter, M. D., Butler, B. J., Gurwell, M. A., 2007. Imaging Uranus at Submillimeter to Centimeter Wavelengths. Bull. Am. Astron. Soc. 39, 424.

Karkoschka, E., Tomasko, M., 2009. The haze and methane distributions on Uranus from HST-STIS spectroscopy. Icarus 202, 287–309.

Karkoschka, E., Tomasko, M. G., 2011. The haze and methane distributions on Neptune from HST-STIS spectroscopy. Icarus 211, 780–797.

Kasten, F., 1969. Visibility forecast in the phase of pre-condensation. Tellus, 631–635.

Krist, J., 1995. Simulation of HST PSFs using Tiny Tim. In: Shaw, R. A., Payne, H. E., Hayes, J. J. E. (Eds.), Astronomical Data Analysis Software and Systems IV. Vol. 77 of Astronomical Society of the Pacific Conference Series. pp. 349–352.

Lebeau, R. P., Dowling, T. E., 1998. EPIC Simulations of Time-Dependent, Three-Dimensional Vortices with Application to Neptune's Great Dark Spot. Icarus 132, 239–265.

Lindal, G. F., Lyons, J. R., Sweetnam, D. N., Eshleman, V. R., Hinson, D. P., 1987. The atmosphere of Uranus - Results of radio occultation measurements with Voyager 2. J. Geophys. Res. 92, 14987–15001.

Pilat, M. J., Charlson, R. J., 1966. Theoretical and optical studies of humdity effects on the size distribution of a hygroscopic aerosol. Journal de Rcherches Atmosphèriques.

Seidelmann, P. K., Abalakin, V. K., Bursa, M., Davies, M. E., de Bergh, C., Lieske, J. H., Oberst, J., Simon, J. L., Standish, E. M., 2002. Report of the IAU/IAG Working Group on Cartographic Coordinates and Rotational Elements of the Planets and Satellites. Celestial Mechanics and Dynamical Astronomy 82, 83–110.

Showman, A. P., de Pater, I., 2005. Dynamical implications of Jupiter's tropospheric ammonia abundance. Icarus 174, 192–204.

Sromovsky, L. A., 2005a. Accurate and approximate calculations of Raman scattering in the atmosphere of Neptune. Icarus 173, 254–283.

Sromovsky, L. A., 2005b. Effects of Rayleigh-scattering polarization on reflected intensity: a fast and accurate approximation method for atmospheres with aerosols. Icarus 173, 284–294.

Sromovsky, L. A., Fry, P. M., 2005. Dynamics of cloud features on Uranus. Icarus 179, 459–484.

Sromovsky, L. A., Fry, P. M., 2010. The source of 3-μm absorption in Jupiter's clouds: Reanalysis of ISO observations using new NH_3 absorption models. Icarus 210, 211–229.

Sromovsky, L. A., Fry, P. M., Hammel, H. B., Ahue, W. M., de Pater, I., Rages, K. A., Showalter, M. R., van Dam, M. A., 2009. Uranus at equinox: Cloud morphology and dynamics. Icarus 203, 265–286.

Sromovsky, L. A., Fry, P. M., Hammel, H. B., de Pater, I., Rages, K. A., 2012. Post-equinox dynamics and polar cloud structure on Uranus. Icarus 220, 694–712.

Sromovsky, L. A., Fry, P. M., Kim, J. H., 2011. Methane on Uranus: The case for a compact CH_4 cloud layer at low latitudes and a severe CH_4 depletion at high latitudes based on re-analysis of Voyager occultation measurements and STIS spectroscopy. Icarus 215, 292–312.

Sun, Z., Schubert, G., Stoker, C. R., 1991. Thermal and humidity winds in outer planet atmospheres. Icarus 91, 154–160.

Sussman, M., Dowling, T. E., Greathouse, T. K., Chanover, N. J., 2012. Seasonal Circulation Modeling of Uranus. In: AAS/Division for Planetary Sciences Meeting Abstracts. Vol. 44 of AAS/Division for Planetary Sciences Meeting Abstracts. p. #504.02.

Tice, D. S., Irwin, P. G. J., Fletcher, L. N., Teanby, N. A., Hurley, J., Orton, G. S., Davis, G. R., 2013. Uranus' cloud particle properties and latitudinal methane variation from IRTF SpeX observations. Icarus 223, 684–698.

Walsh, J. R., Goudfrooij, P., Malumuth, E., 2001. STIS Geometric Distortion - SMOV3A tests for CCD, NUVMAMA and FUV-MAMA. Tech. rep.

Supplemental material.

Three files are included as supplementary material. The hyperspectral cube containing calibrated I/F values as a function of wavelength and location, with a navigation back plane that provides viewing geometry and latitude-longitude coordinates for each pixel, is provided in ura_stis12_wfc3cal_navbp.fits. A detailed explanation of the contents of this file is provided in the file README_SUPPLEMENTAL.TXT. A sample IDL program that reads the cube file, plots a monochromatic image, extracts data from a particular location on the disc, and plots a spectrum, is provided in the file stis_cube_example.pro. The IDL astronomy library will be needed to read the data cube, which is in the FITS format.

Table 1: Science exposures from HST program 12894. All STIS spectra used the $52'' \times 0.1''$ slit.

Orbit	Start Date (UTH)	Start Time (UTH)	Instrument	Filter or Grating	Exposure (sec)	No. of Exp.	Phase Angle (°)
1	2012-09-27	21:22:29	STIS	MIRVIS	10.1	1	0.09
1	2012-09-27	21:38:11	STIS	G430L	70.0	13	0.09
2	2012-09-27	22:56:43	STIS	G750L	86.0	18	0.08
3	2012-09-28	00:32:26	STIS	G750L	86.0	18	0.08
4	2012-09-30	22:44:50	WFC3	F336W	30.0	1	0.09
4	2012-09-30	22:46:35	WFC3	F467M	16.0	1	0.09
4	2012-09-30	22:48:15	WFC3	F547M	6.0	1	0.09
4	2012-09-30	22:49:39	WFC3	F631N	65.0	1	0.09
4	2012-09-30	22:52:08	WFC3	F665N	52.0	1	0.09
4	2012-09-30	22:54:15	WFC3	F763M	26.0	1	0.09
4	2012-09-30	22:56:02	WFC3	F845M	35.0	1	0.09
4	2012-09-30	22:57:56	WFC3	F953N	250.0	1	0.09
4	2012-09-30	23:04:27	WFC3	FQ889N	450.0	1	0.09
4	2012-09-30	23:16:02	WFC3	FQ937N	160.0	1	0.09
4	2012-09-30	23:23:05	WFC3	FQ727N	240.0	1	0.09

On September 28 the observer range was 19.0613 AU (2.851530×10^9 km) and the equatorial angular diameter of Uranus was 3.6976 arcseconds.

Table 2: Point spread function (PSF) for final calibrated data cube.

0	0	-11	-22	-20	-22	-11	0	0
0	-19	55	400	615	400	55	-19	0
-11	55	894	2370	3168	2370	894	55	-11
-22	400	2370	5458	7058	5458	2370	400	-22
-20	615	3168	7058	9048	7058	3168	615	-20
-22	400	2370	5458	7058	5458	2370	400	-22
-11	55	894	2370	3168	2370	894	55	-11
0	-19	55	400	615	400	55	-19	0
0	0	-11	-22	-20	-22	-11	0	0

Table 3: Compact cloud model parameters

	Parameter/function	Value
Stratospheric haze of Mie particles with gamma size distribution	$m1\_pd$ (bottom pressure)	fixed at 100 mb
	$m1\_r$ (particle radius)	fixed at 0.1 μm
	$m1\_b$ (variance)	fixed at 0.3
	$n1$ (refractive index)	nr=1.4, ni given by Eqn. 3
	$m1\_odpb$ (optical depth/bar)	adjustable1
Upper tropospheric haze of double HG particles (UTH)	$hg1\_pd$ (bottom pressure)	fixed at 0.9 bars (top pressure = m1_pd)
	$\varpi(\lambda)$ (single-scatt. albedo)	Eqn. 4
	phase function (KT2009)	$g_1 = 0.7$, $g_2 = 0.3$, $f_1(\lambda)$ given by Eqn. 5
	$hg1\_odpb$ (optical depth/bar)	adjustable2
Upper middle tropospheric cloud layer of Mie particles (UMTC)	$m2\_p$ (bottom pressure)	adjustable3 (top pressure = m2_p x 0.9)
	$m2\_r$ (particle radius)	adjustable4
	$m2\_b$ (variance)	fixed at 0.3
	$n2$ (refractive index)	fixed at n=1.4
	$m2\_od$ (optical depth)	adjustable5
Lower middle tropospheric cloud of double HG particles (LMTC)	$hg2\_p$ (bottom pressure)	fixed or adjustable8 (Ptop = hg2_p X 0.9)
	$\varpi(\lambda)$ (single-scatt. albedo)	Eqn. 4
	phase function (KT2009)	$g_1 = 0.7$, $g_2 = 0.3$, $f_1(\lambda)$ given by Eqn. 5
	$hg2\_od$ (optical depth)	adjustable6
Bottom tropospheric cloud (BTC)	$\varpi(\lambda)$	same as previous layer
	phase function (DHG)	same as previous layer
	$hg3\_od$ (optical depth)	adjustable7
	$hg3\_p$ (bottom pressure)	fixed at 5 bars

Table 4: Best-fit parameters for equatorial compact cloud layer models versus latitude assuming simulated F1 profile for latitudes between 30° S and 30° N, and using depleted F1 profiles for higher latitudes.

Lat. °	*m*2_*p* bar	*hg*2_*p* bar	*m*1_*od pb*	*m*2_*od*	*hg*2_*od*	*hg*3_*od*	*m*2_*r* μm	χ^2	(m-o)/u
-30	1.22±0.03	1.42±0.02	0.13±0.05	0.41±0.10	0.90±0.06	3.97±0.8	0.31±0.08	312	-0.46
-20	1.29±0.03	1.53±0.03	0.05±0.04	0.40±0.08	0.90±0.07	2.73±0.7	0.18±0.02	319	0.68
-10	1.24±0.02	1.53±0.03	0.18±0.04	0.43±0.08	1.01±0.07	3.94±0.8	0.17±0.01	284	0.71
0	1.17±0.01	1.52±0.04	0.36±0.03	0.39±0.06	1.16±0.07	2.77±0.6	0.57±0.04	230	-0.27
10	1.25±0.02	1.49±0.03	0.15±0.04	0.44±0.08	1.05±0.07	4.35±0.9	0.15±0.01	282	0.94
20	1.24±0.02	1.49±0.03	0.02±0.15	0.43±0.08	1.08±0.07	4.49±1.0	0.17±0.01	326	0.23
30	1.19±0.03	1.36±0.02	0.00±0.00	0.17±0.03	0.94±0.04	4.27±0.6	0.17±0.02	227	0.69
38	1.30±0.04	1.68±0.03	0.00±0.00	0.45±0.10	0.91±0.05	2.17±0.5	0.31±0.04	252	0.45
45	1.26±0.05	1.57±0.02	0.00±0.00	0.40±0.08	1.04±0.05	1.84±0.5	0.26±0.04	347	0.04
50	1.27±0.05	1.63±0.02	0.00±0.00	0.33±0.05	1.05±0.04	1.33±0.3	0.21±0.03	242	-0.15
60	1.29±0.06	1.78±0.04	0.00±0.00	0.40±0.08	0.83±0.05	0.05±1.9	0.33±0.05	263	0.05
70	1.42±0.06	1.93±0.07	0.00±0.00	0.50±0.10	0.67±0.04	0.00±0.00	0.36±0.05	260	0.20

Note: The fits from -30° to 30° were done using the F1 thermal and methane profile, which has a deep methane volume mixing ratio of 4%, and a He/H_2 ratio of 0.1306. At other latitudes the fits used methane depleted profiles with *vx*=2.0 and depletion depths that minimized the 825-nm errors (listed in Table 5 and plotted in Fig. 22) The uncertainty in χ^2 is ∼25 and thus fits differing by less than this are not of significantly different quality. The column labeled $(m-o)/u$ is the fit error at 0.825 μm expressed as the ratio of (model I/F - observed I/F) to the estimated I/F uncertainty for μ = 0.6. These results are plotted in Fig. 22.

Table 5: Optimum depletion depth based on fit quality and 825-nm error as a function of depletion profile rate (small *vx* provides sharper depletions above the depletion depth limit p_d).

Planetographic		minimum χ^2			minimum 825-nm error		
Latitude, °	*vx*	p_d	χ^2	825-nm error	p_d, bars	825-nm error	χ^2
60	0.5	2.0	376.87	-1.0	2.5	0.04	514.47
60	1.0	3.0	320.29	-0.55	3.5	-0.07	332.77
60	1.5	5.5	281.80	0.19	5.0	0.00	281.90
60	2.0	10.0	255.94	0.58	7.5	0.05	262.55
60	3.0	30	245.20	0.76	16	-0.08	255.66
60	5.0	200	262.57	0.59	90	0.01	263.55
38	2.0	1.5	231.94	-1.11	3.0	0.45	252.17
45	2.0	1.5	334.78	-1.34	3.0	0.04	347.30
50	2.0	4.0	242.01	-0.15	4.0	-0.15	242.01
70	2.0	10	259.78	0.20	10	0.20	259.78

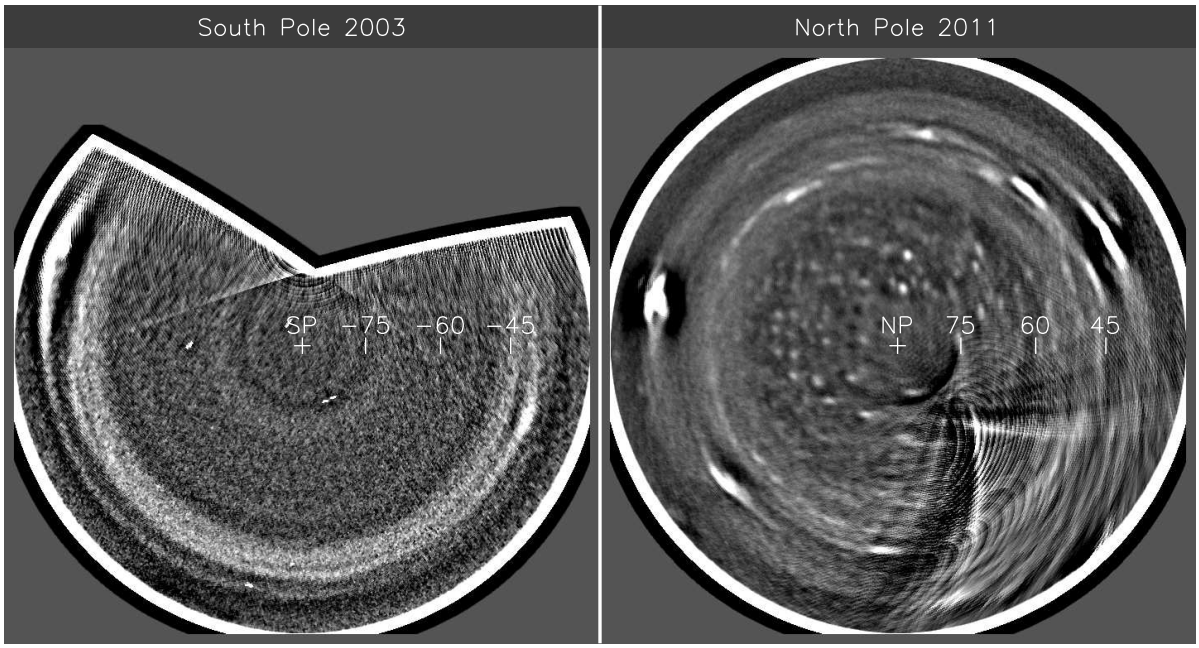

Figure 1: Shift-and-add high-pass filtered projections of Uranus' 2003 South (L) and 2011 North (R) polar regions reveal a large asymmetry in cloud features poleward of 45°, suggesting very different degrees of polar convection, a likely seasonal effect (Sromovsky et al. 2012). The images were obtained with the Keck 2 telescope and NIRC2 instrument using an H filter (1.62 μm central wavelength).

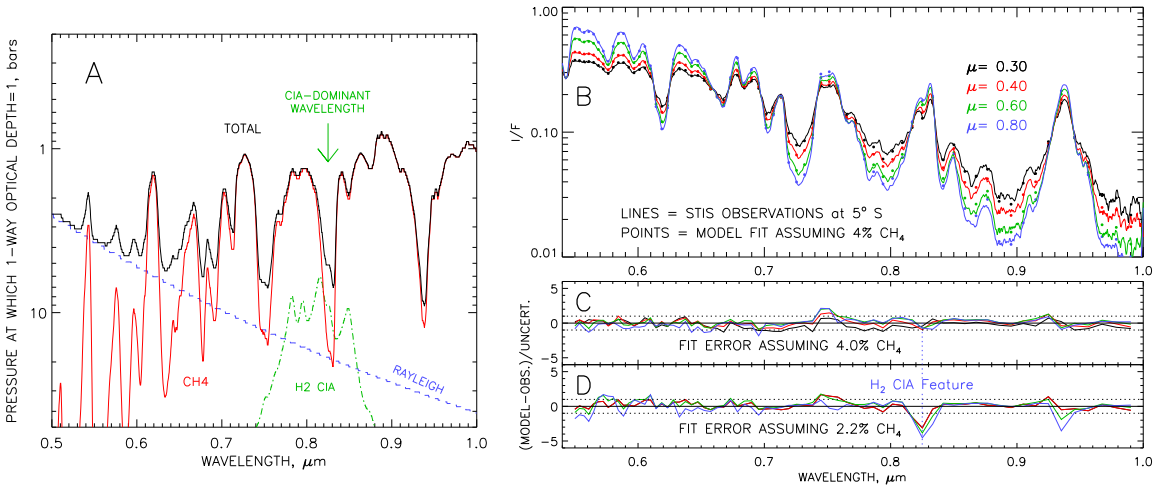

Figure 2: A: Penetration depth vs. wavelength as limited by different opacity sources assuming the F1 methane profile and absorption models discussed in Sec. 6.1. Note the greater importance of H_2 CIA near 825 nm. The dark solid curve includes all absorbers, while the other curves are for single absorbers in isolation. B: Example model fit for the F1 profile of Sromovsky et al. (2011) with a deep methane volume mixing ratio of 4%, and fit errors for deep methane mixing ratios of 4% (C) and 2.2% (D). The fit errors near 825 nm are a sensitive indicator of the mixing ratio of CH_4 to H_2.

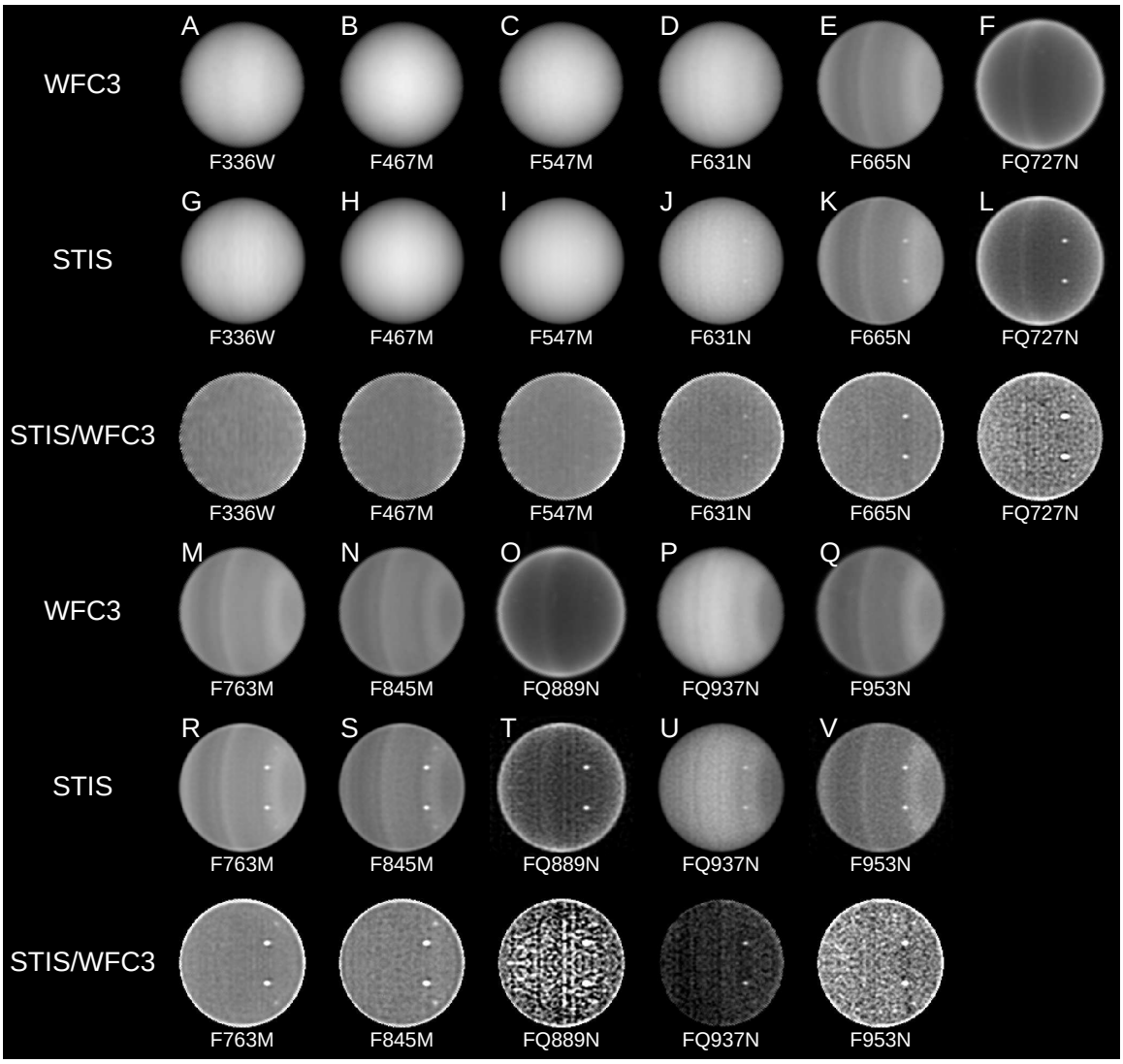

Figure 3: WFC3 images of Uranus taken on 30 September 2012 (A-F and M-Q) compared to synthetic band-pass filter images (G-L and S-W) created from weighted averages of STIS spectral data cubes using WFC3 throughput and solar spectral weighting. The north pole is at at the right. Portions of the synthetic images east of the central meridian are obtained by reflection of the images west of the central meridian. That is why the single cloud feature appears twice in images where cloud contrast is sufficient to make the cloud visible. The STIS data were acquired three days before the WFC3 data, which were taken when the discrete cloud was not visible. The ratio images are stretched to make 0.8 black and 1.2 white. For a direct comparison of latitude scans at fixed view angles, see Fig. 5.

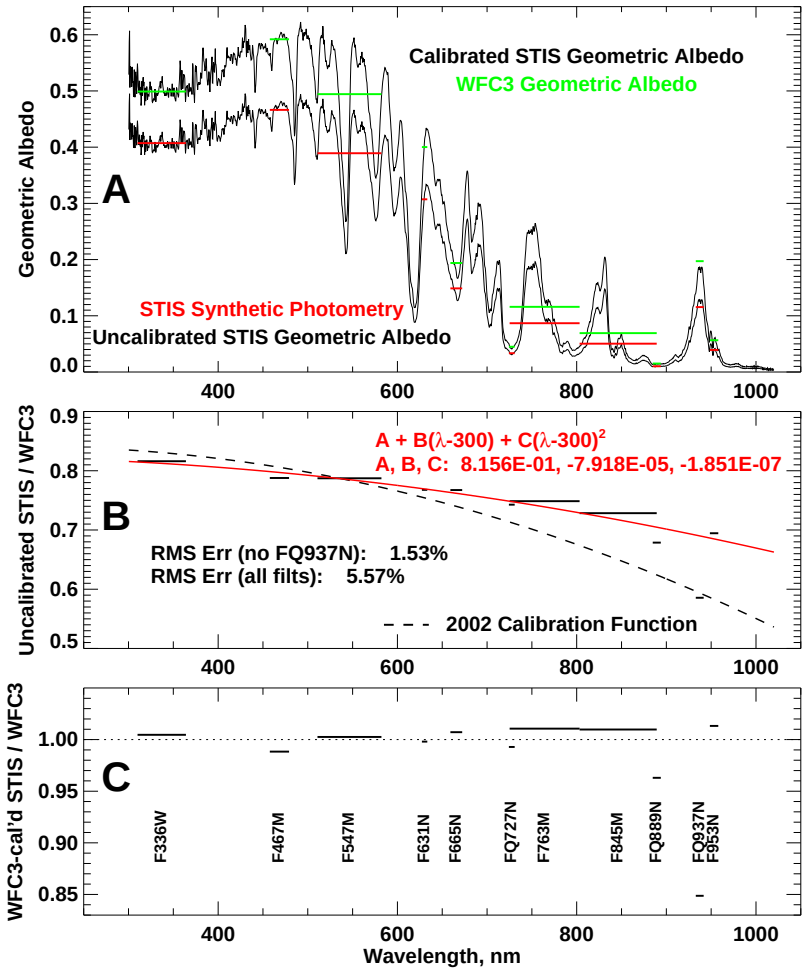

Figure 4: A: Disk-integrated I/F spectra before final calibration (lower curve) and after final calibration (upper curve), where horizontal red bars indicate synthetic I/F values computed from pre-calibration spectra and horizontal green bars indicate I/F values obtained from WFC3 imaging. B: Synthetic band-pass filter disk-integrated I/F values (pre-calibration) divided by corresponding I/F values obtained from WFC3 measurements (horizontal bars). The red (solid) curve and legend coefficients defining it, were obtained by fitting all ratio values except that obtained from the FQ937N filter. The black (dashed) curve is the calibration function obtained from the 2002 data set. C: Ratio of synthetic disk-integrated I/F values obtained from calibrated STIS spectra to the corresponding WFC3 values.

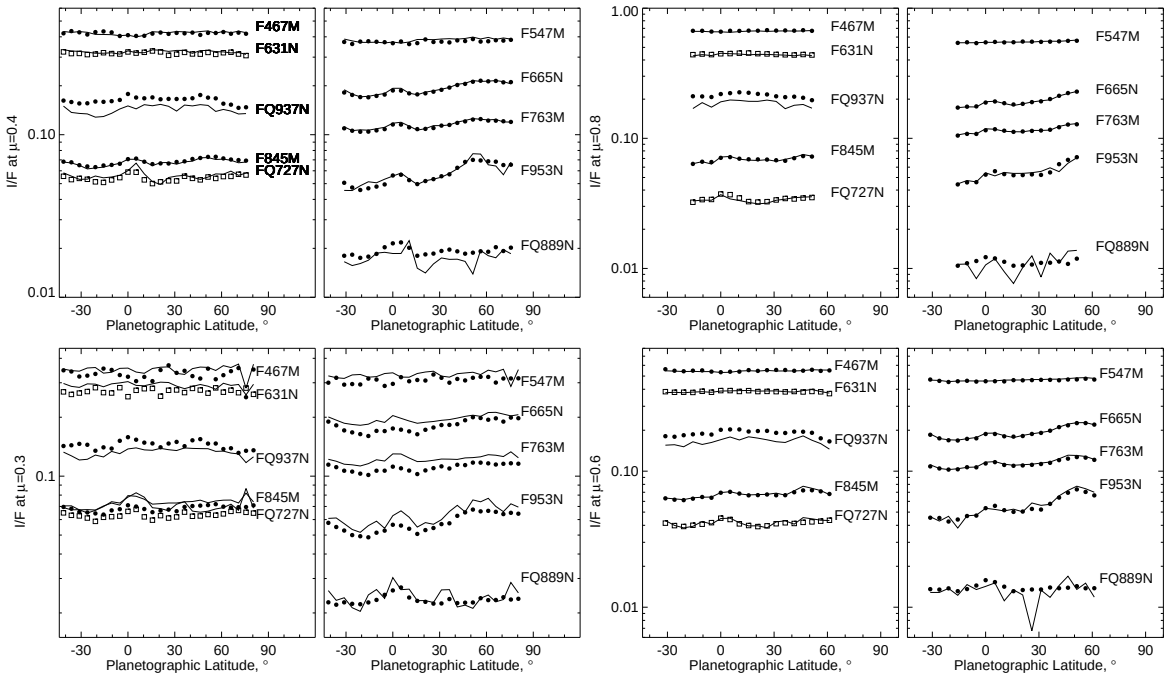

Figure 5: Comparison of WFC3 (symbols) and STIS synthetic WFC3 (lines) vs. latitude at fixed solar zenith angle cosines of 0.3 (LL), 0.4 (UL), 0.6 (LR), and 0.8 (UR), for each of the 11 filters used. These I/F values are obtained from the synthetic images by unsmoothed interpolation, and slightly different results would be obtained from CTL fits described in the text.

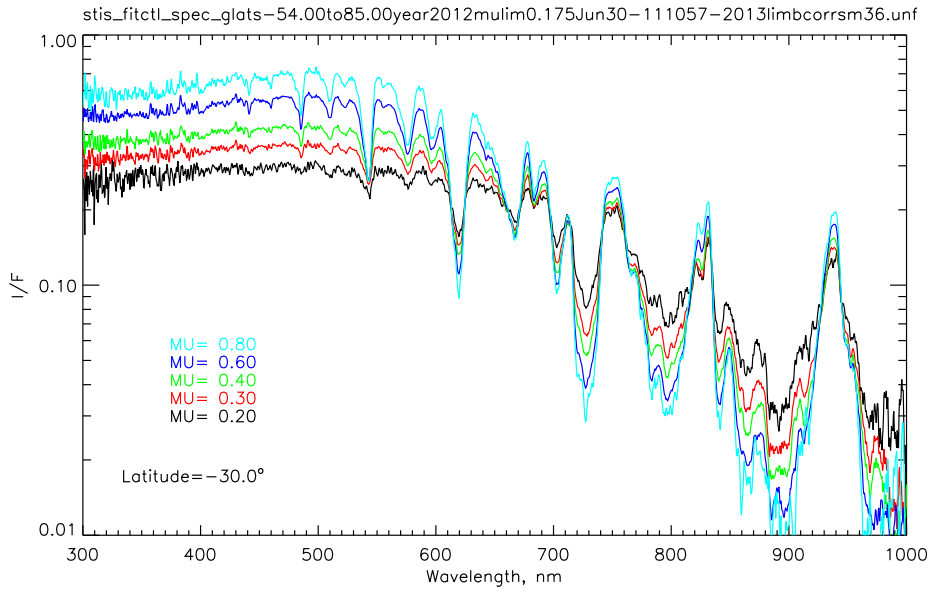

Figure 6: Sample spectra with 36 cm^{-1} smoothing in the wavenumber domain, which provides uniform wavenumber resolution needed for Raman calculations and also produces a significant reduction of noise at longer wavelengths. Note the general trend of limb darkening at continuum wavelengths, and limb brightening at the strongly absorbing wavelengths.

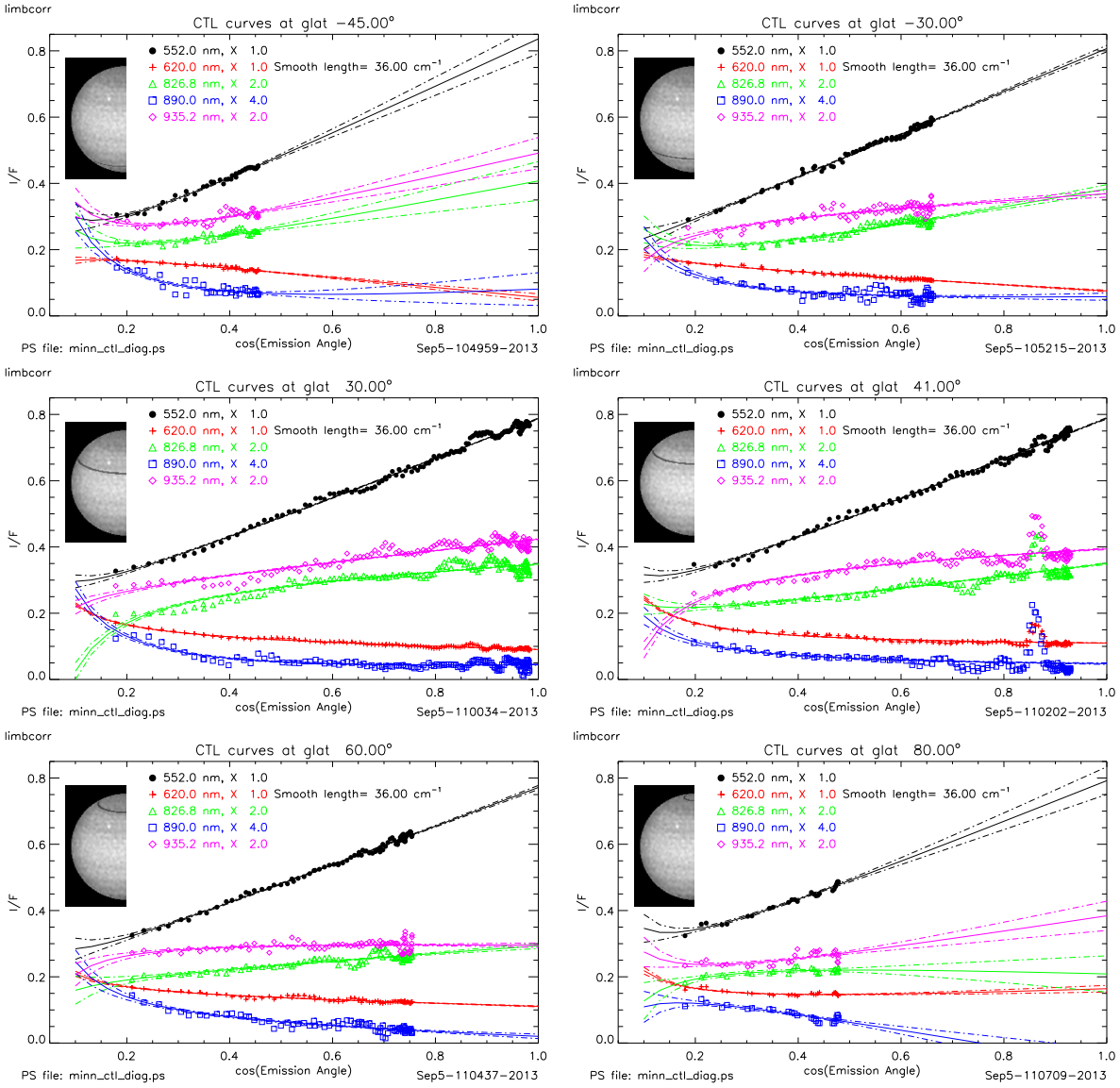

Figure 7: Sample center-to-limb fits at six different latitudes as described in the main text. Each panel shows STIS I/F samples and fit lines with uncertainty bands for five different wavelengths indicated in the legends. In each panel the latitude band sampled for each fit is darkened in the inset image of the half-disk of Uranus. Note that the fits for 41° N are not much disturbed by the cloud feature near μ=0.87.

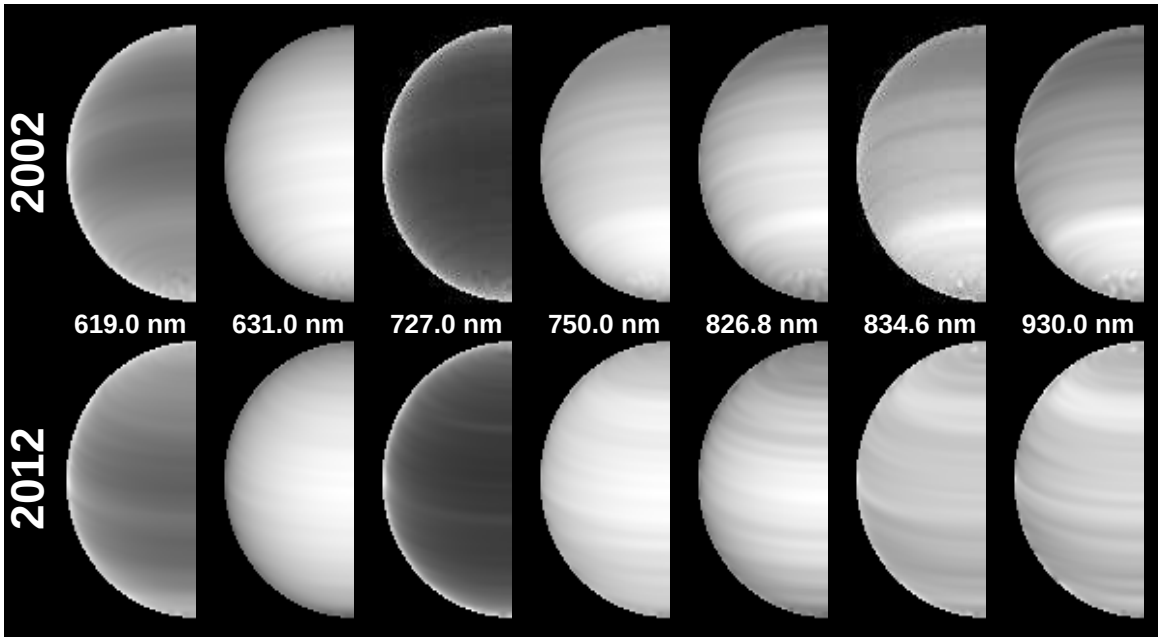

Figure 8: Comparison of 2002 and 2012 synthetic images created from CTL fits for six sample wavelengths (these are autoscaled)). Note that the images for the H_2 CIA-dominated wavelength (826.8 nm) have relatively bright low latitudes and darker polar regions, while the images for the methane dominate wavelength of 930 nm do not. This implies that there is relatively less methane absorption (compared to H_2 absorption) at high latitudes. Note that the longitudinal structure seen near the poles, a region where CTL fits did not replace the original image data, is mostly due to noise.

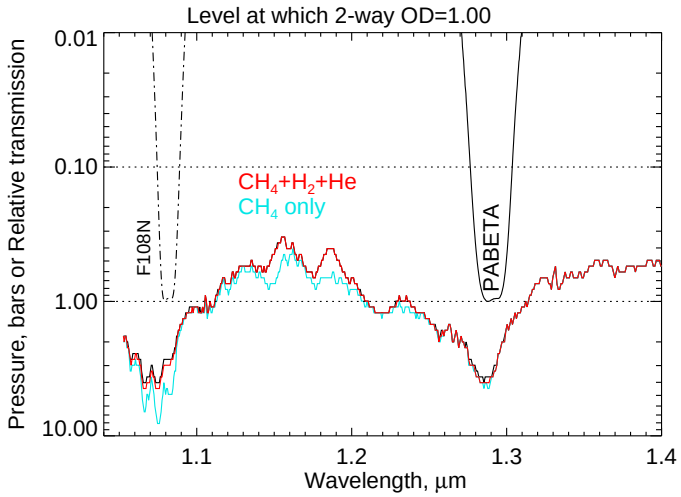

Figure 9: Near-IR penetration depths vs. wavelength compared to filter transmission for F108N NICMOS and PaBeta Keck/NIRC2 filters, which sense similar atmospheric levels in a clear atmosphere, but are dominated by different gas absorptions (H_2 and CH_4 respectively).

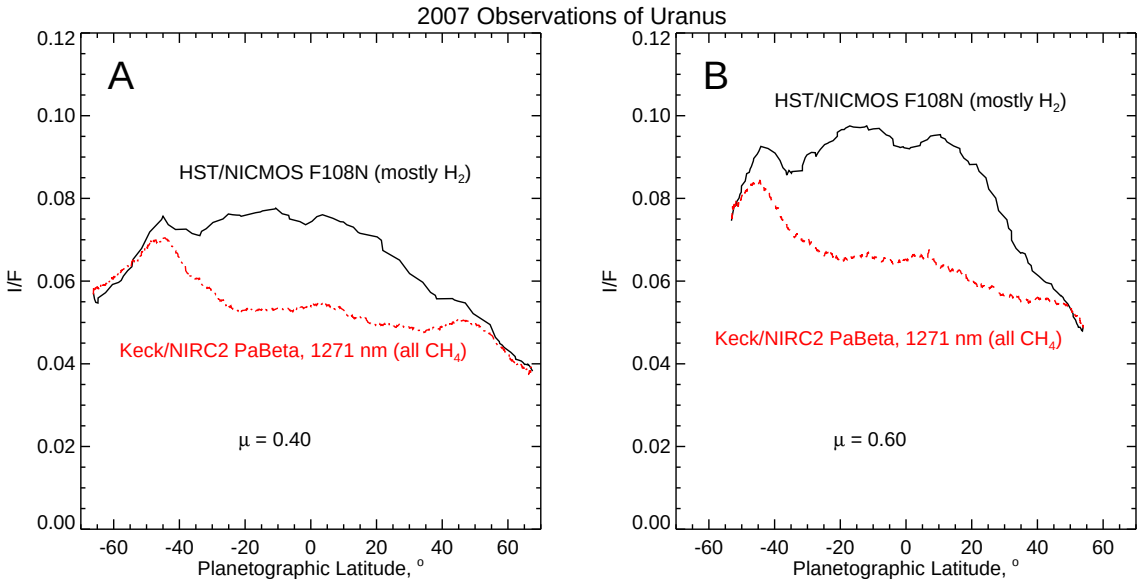

Figure 10: Latitudinal profiles at fixed zenith angle cosines of 0.4 (A) and 0.6 (B) for F108N and PaBeta (Keck/NIRC2) filters taken near the Uranus equinox in 2007. At this point the southern hemisphere was still generally brighter than the northern hemisphere and the 38° S - 58° S southern bright band was still better defined and considerably brighter than the corresponding northern bright band. The relatively low equatorial I/F values for the methane-dominated PaBeta filter band indicates increased CH_4/H_2 absorption at low latitudes.

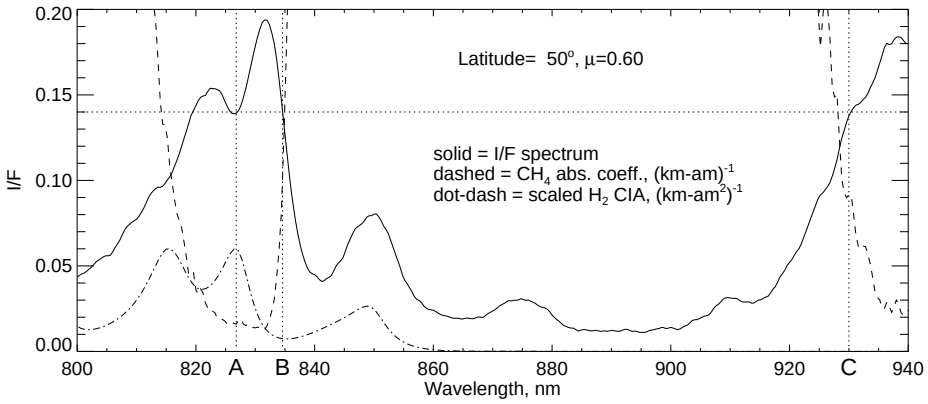

Figure 11: I/F and absorption spectra comparing the equilibrium H_2 CIA coefficient spectrum (divided by 1.2e-7, shown as dot-dash curve) and methane absorption coefficient spectrum (dashed). Note that the I/F spectrum has nearly equal I/F values at 826.8 nm (A), 834.6 nm (B), and 930 nm (C), but H_2 absorption is much greater at A than at B, while the opposite is true of methane absorption, and at C only methane absorption is present. In a reflecting layer model, changes in cloud reflectivity should affect wavelengths A-C by the same factor, but changes in methane mixing ratio would affect C most and A least.

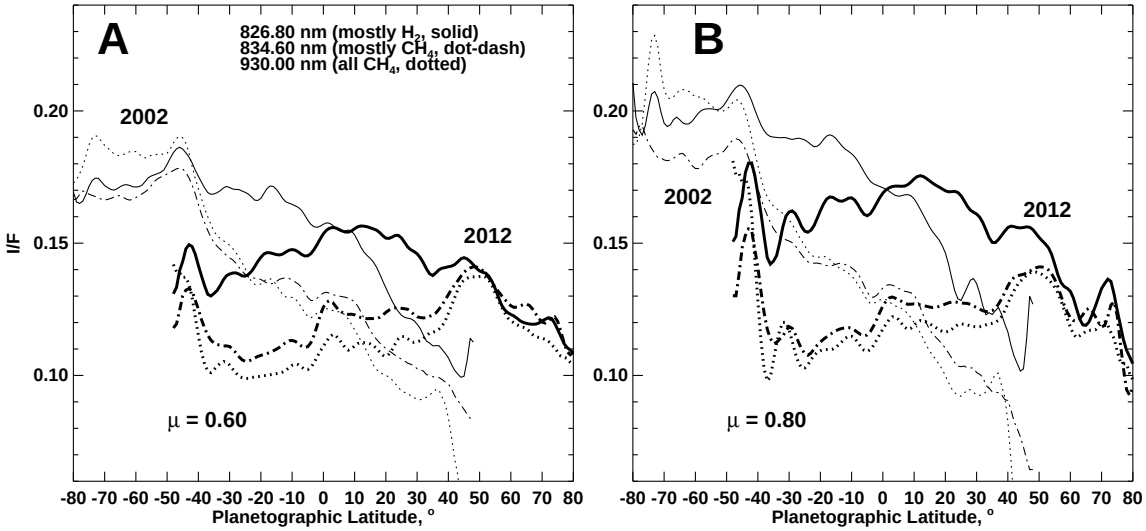

Figure 12: I/F vs latitude at $\mu = 0.6$ (A) and $\mu = 0.8$ (B) for three wavelengths with different amounts of methane and hydrogen absorption. Thin curves are from 2002 and thick curves from 2012. These are plots of center-to-limb fitted values instead of raw image data. In both cases the methane-dominated wavelengths have much reduced I/F at low latitudes. The 2002 calibration is based on WFPC2 comparisons and leads to I/F values 3% lower than the original KT2009 calibration.

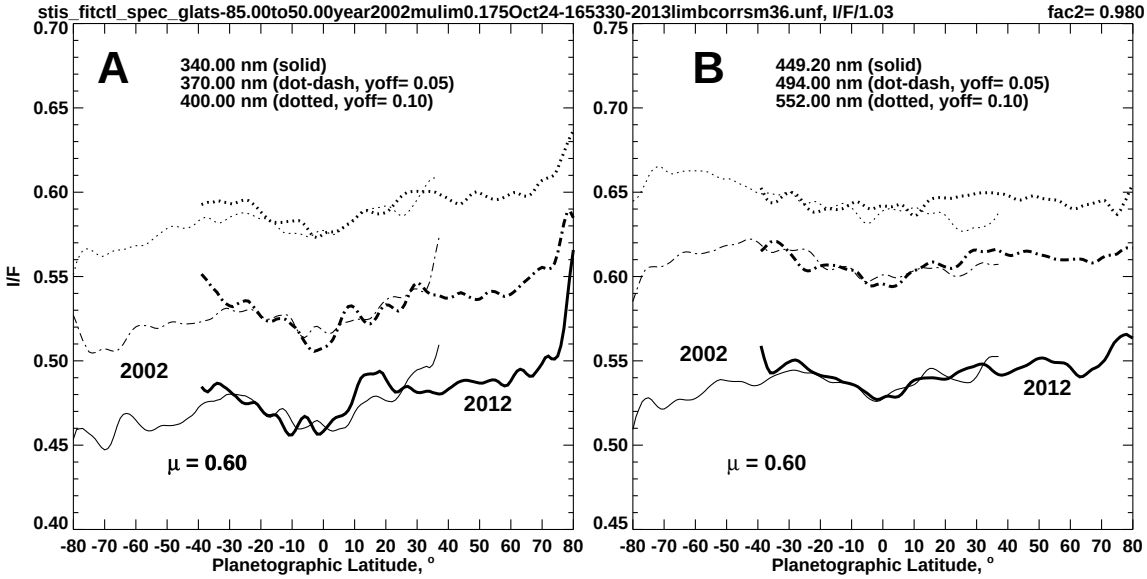

Figure 13: I/F vs latitude for six continuum wavelengths indicated in the legends. Thick curves are for 2012 and thin curves for 2002. These are plots of center-to-limb fitted values instead of raw image data. The 2002 I/F values were multiplied by 0.98 to provide the best match with 2012 values in the overlap region. Most of the change seen at continuum wavelengths is likely due to calibration differences between 2002 and 2012 .

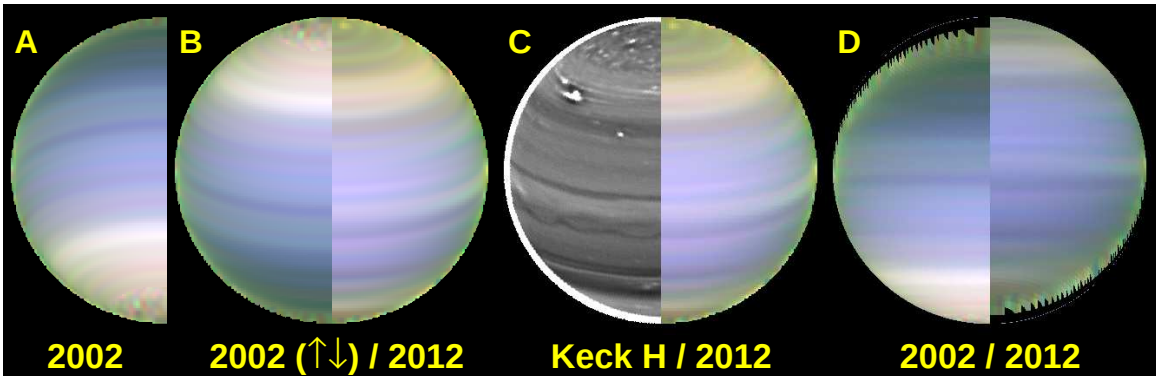

Figure 14: Color composites of fitted center-to-limb smoothed images for 2002 (**A, B, D**) and 2012 (**B-D**) using color assignments R = 930 nm (all methane), G = 834.6 nm (methane and hydrogen), and B = 826.8 nm (mostly hydrogen). North is up in all images except the reflected 2002 image in **B**. The blue tint at low latitudes for both years is due to locally increased methane absorption. In **B** the 2002 image is inverted after remapping to the same central latitude as the 2012 image. The obvious asymmetry is not surprising because Uranus was in southern summer in 2002 and northern spring in 2012. In **C** we compare 2012 STIS observations with a Keck/NIRC2 near-IR image taken in the same year, high-pass filtered to enhance cloud structure. Note the small cloud features north of the bright band. In **D** we compare 2002 and 2012 STIS observations at the same latitudes (i.e. without reflection of 2002 about the equator) and with both observations remapped to place the equator at the center of the image. In **D** the enhancement is the same for both 2002 and 2012, but using the 2012 albedo calibration function for both data sets (the solid curve in Fig. 4). The southern high latitudes in 2002 were brighter and whiter than in 2012, providing evidence for a seasonal lag. The dark band near the center of the two images is 5° south of the equator. A comparison of latitudinal variations at fixed view angles is provided in Fig. 12.

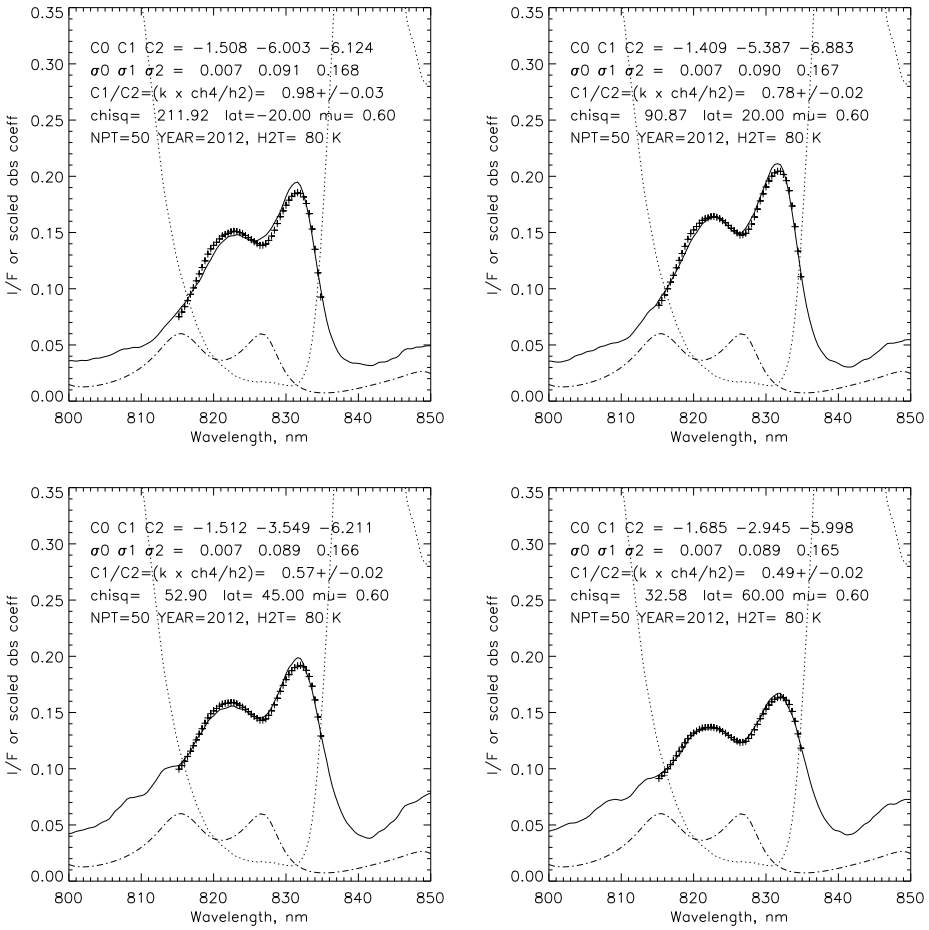

Figure 15: The 2012 I/F spectrum (solid curves) from 815 to 835 nm at μ=0.6 for four sample latitudes (-20°, 20°, 45°, and 60° from left to right and top to bottom), using the simplified model (+) of Eq. 2, as discussed in the text. Relative variations of methane (dotted) and H_2 (dot-dash) absorptions are also shown.

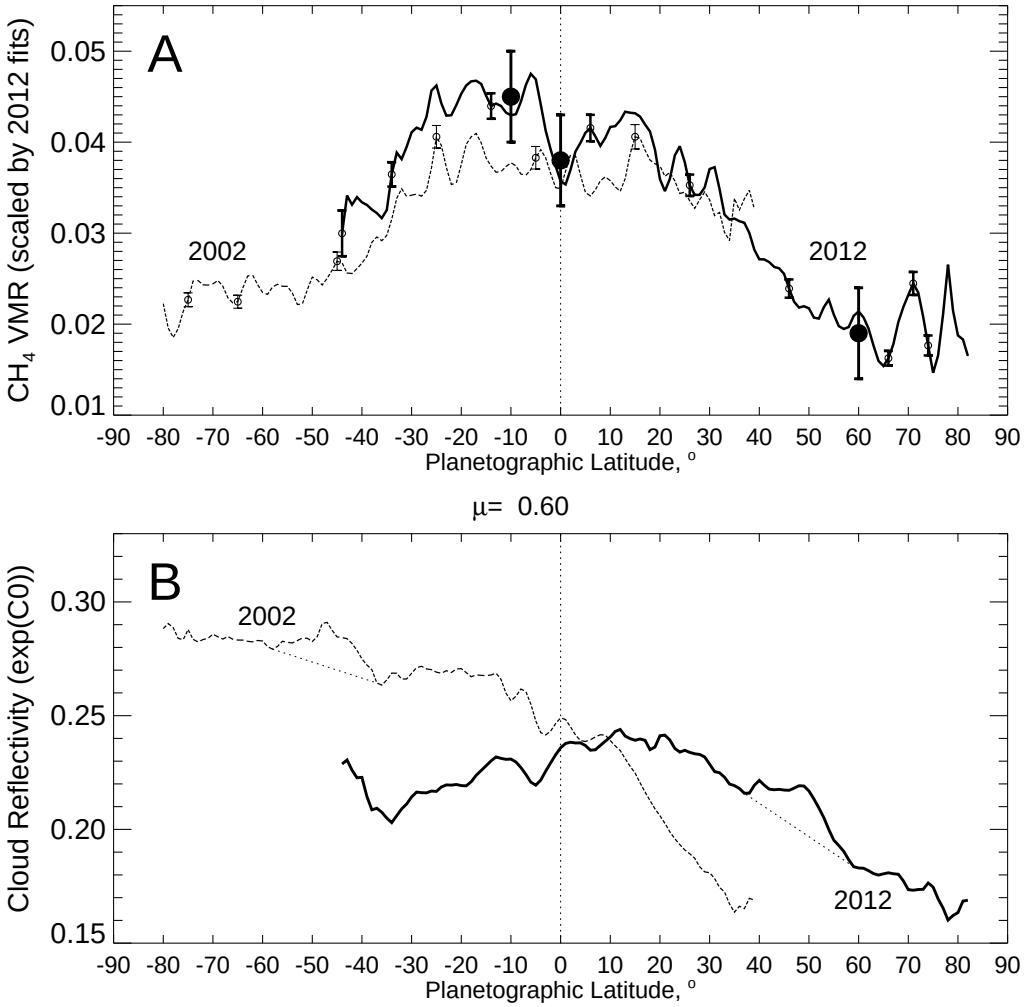

Figure 16: A: Latitude dependence of the ratio C_1/C_2, which is crudely proportional to the CH_4/H_2 mixing ratio, scaled to best match the 2012 CH_4 VMR estimates at 10° S, the equator, and 60° N, obtained from radiation transfer modeling. Those results are plotted as larger filled circles with error bars. The same scaling used on the 2002 data (thin dashed line) leads to a slightly lower methane VMR at low latitudes. Error bars for the C_1/C_2 ratio points are provided only for scattered samples for clarity. B: The aerosol reflectivity term (exp(C0)), for 2002 and 2012, using the KT2009 spectral calibration divided by 1.03 for 2002 results. Dotted lines interpolate across the regions where bright bands are seen (38° - 58°).

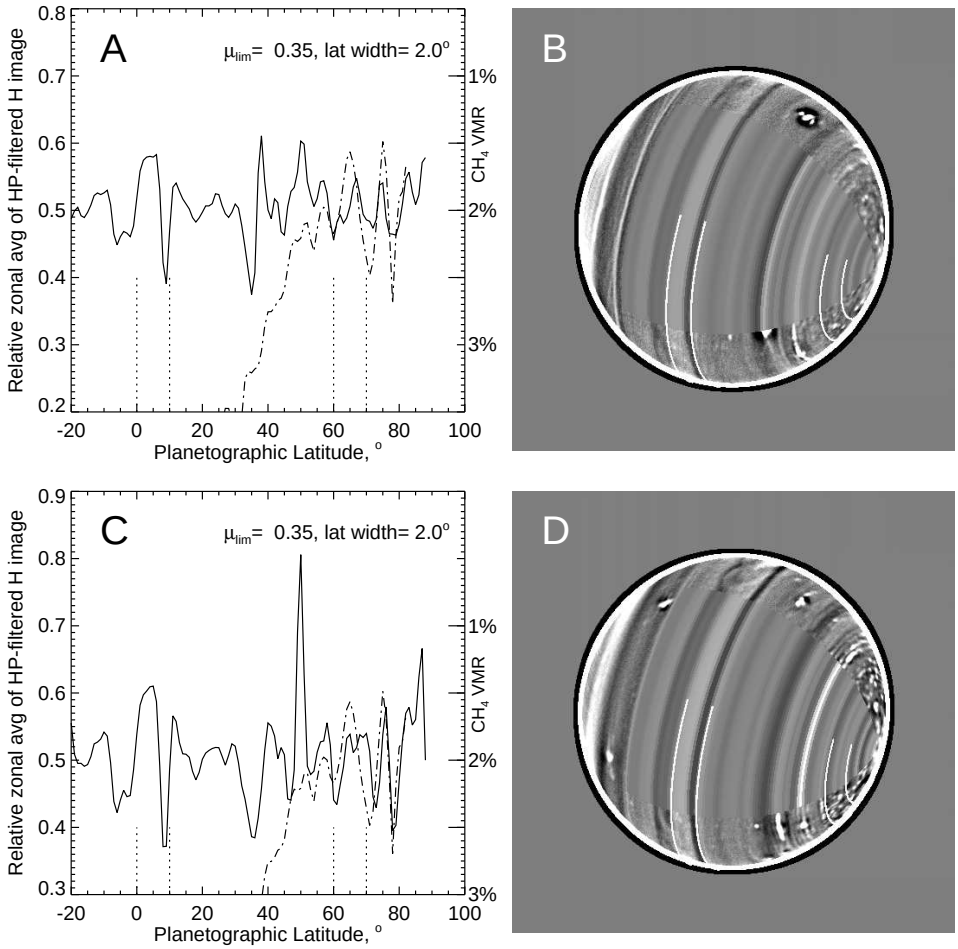

Figure 17: Effective STIS-derived methane mixing ratio vs. latitude profile (dot-dash curves in A, C) from Fig. 16 compared to relative zonal averages (solid curves in A, C) of high-pass filtered high signal-to-noise H-band (1.62 μm) Keck/NIRC2 images from 16 August 2012 (B) and 4 November 2012 (D). In the images in B and D the 90° of pixels that were averaged have been replaced by their longitudinally averaged values. Grid lines at 0°, 10°, 60°, and 70°extend half way across the images in B and D, and vertical dotted lines mark the same latitudes in A and C. Correlations between zonal average variations and effective methane VMR variations from 55° N to 82° N are significant (see text).

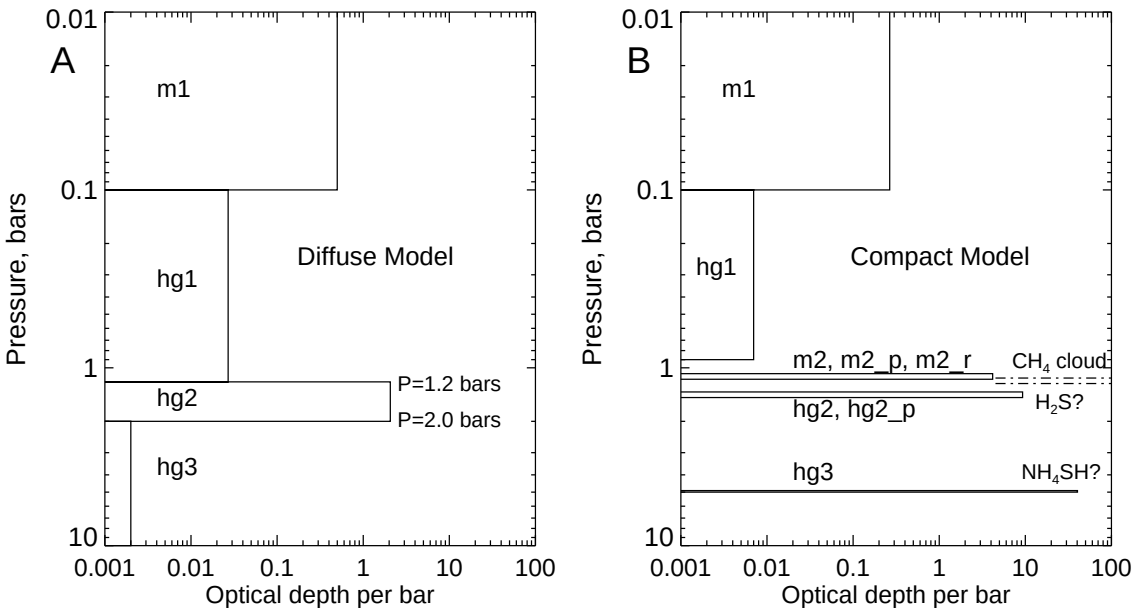

Figure 18: Comparison of diffuse (A) and compact (B) vertical cloud structure models. In A, which illustrates the KT2009 model, the cloud boundaries are fixed and the only adjustable parameters are the optical depths per bar. In B, which illustrates our compact model, there are two layers for which additional adjustable parameters of base pressure (for the new *hg*2 layer) and base pressure and particle radius (for the new *m*2 layer).

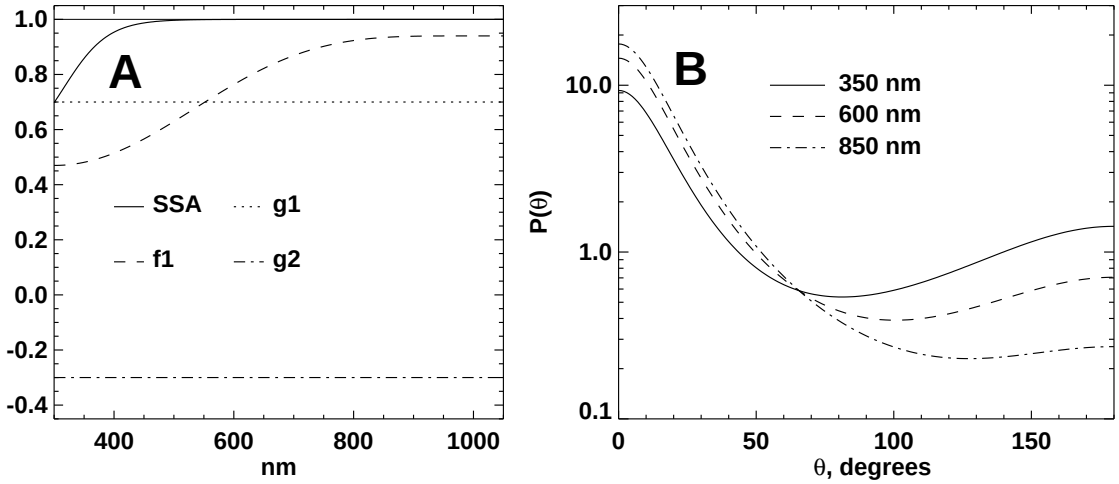

Figure 19: Wavelength dependent functions used in KT2009 cloud models (A) and sample phase functions derived from these parameters (B).

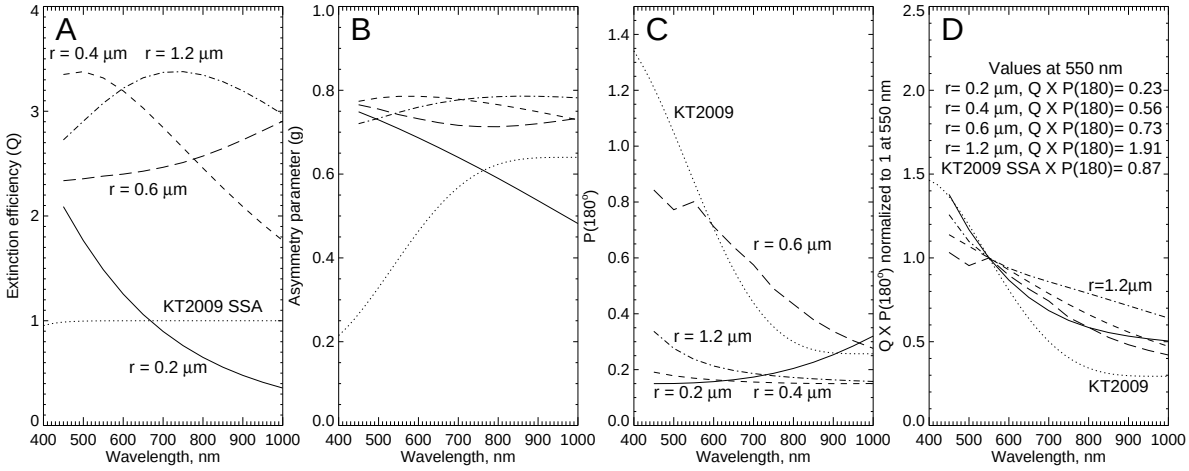

Figure 20: Mie particle scattering properties for four sizes of particles, n=1.4+0i, and a gamma size distribution of variance 0.1. Also shown are KT2009 single-scattering albedo (in A), asymmetry parameter (B), backscatter phase function (C) and backscatter efficiency normalized to unity at 550 nm (D).

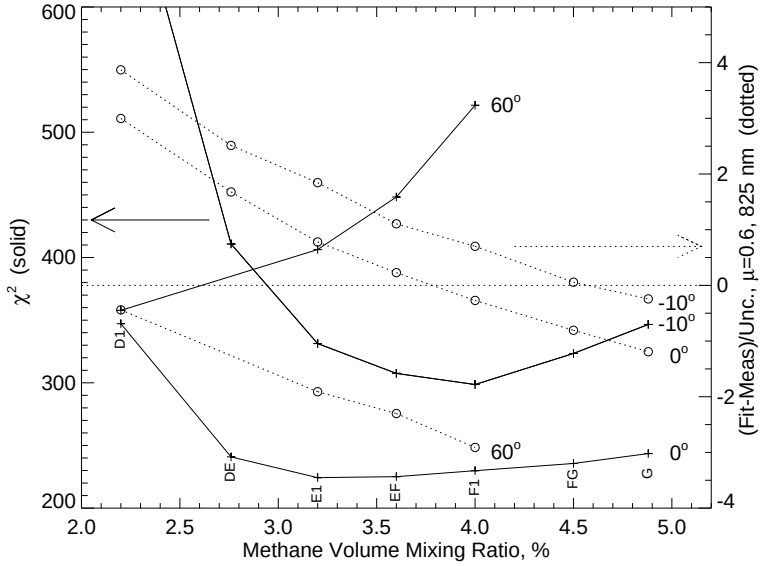

Figure 21: Best-fit compact model parameters vs deep methane mixing ratio for undepleted occultation-consistent D1, E1, EF, F1, and G profiles from Sromovsky et al. (2011), and DE and FG profiles using the same procedure. The fits are to STIS spectra at 10° S, the equator, and 60° N, for zenith angle cosines of 0.3, 0.4, and 0.6. The χ^2 values are shown with solid curves, and the 825-nm error ratio to expected error at μ=0.6 is shown with dotted curves. Horizontal arrows indicate which axis to read in each case.

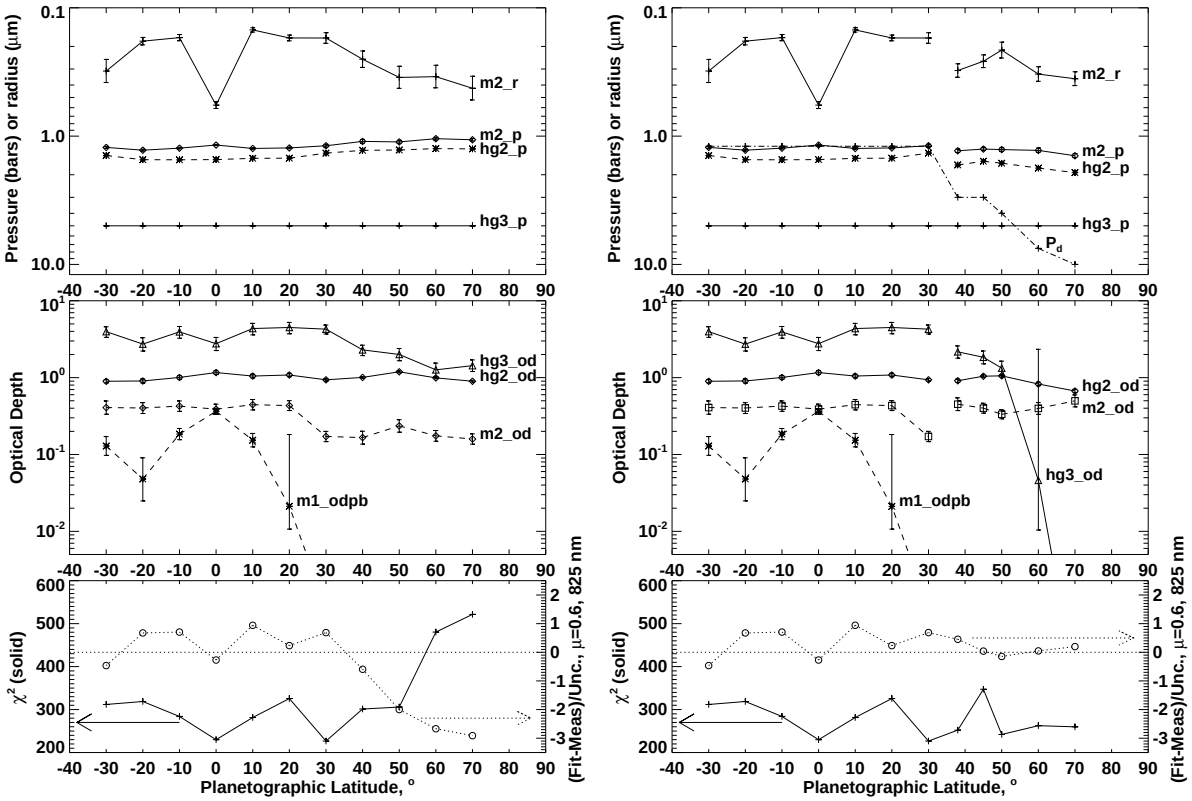

Figure 22: Best-fit compact model parameters vs. latitude assuming the F1 structure and methane mixing ratio profile (left) and using the best-fit depletion depth profiles (right). Error bars indicate fitting uncertainty. In each case, the lower panel displays fit quality in terms of χ^2 (+) and signed 825-nm error (o). In the bottom left plot, the behavior of the 825-nm error indicates that the actual methane absorption declines below the assumed value beginning about 40° N. In the bottom right plot, both 825-nm error and χ^2 benefit from use of depleted profiles. In the bottom panels horizontal arrows indicate which axis to read for each curve.

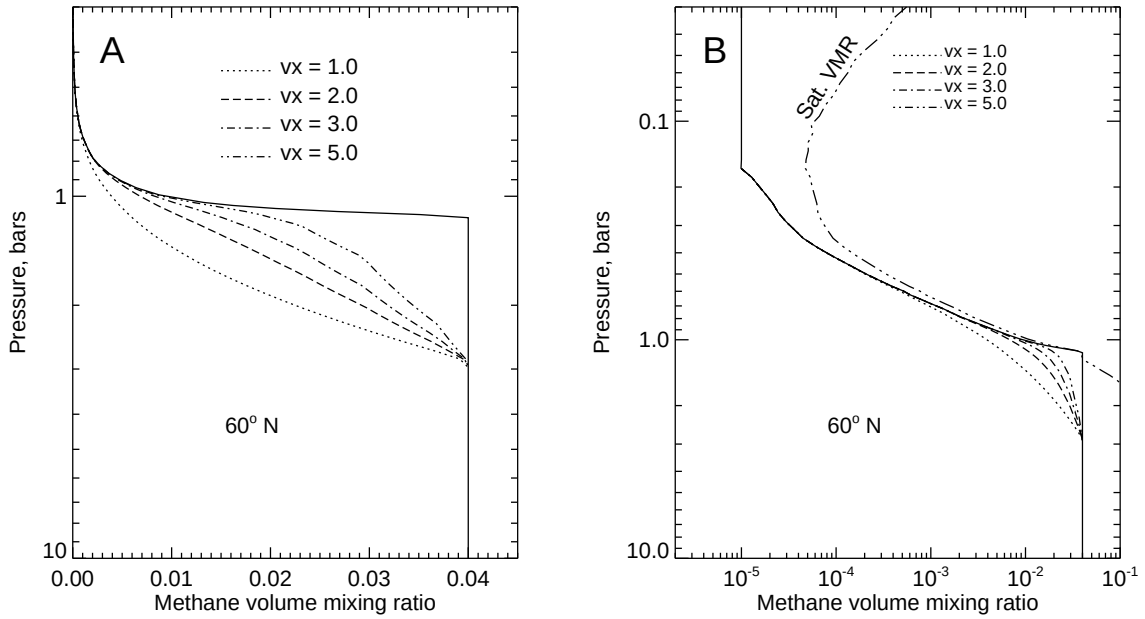

Figure 23: (A): Sample depletion functions of methane mixing ratio vs. pressure for P_d=3 and different values of *vx*. (B): sample profiles vs. log of the mixing ratio in comparison with the saturation mixing ratio profile.

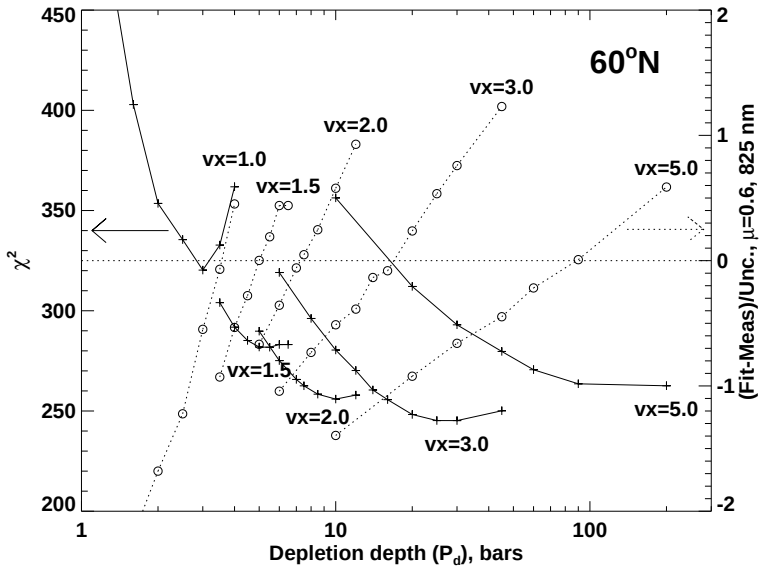

Figure 24: Fit quality estimates for compact cloud layer model fits to spectra at 60° N (χ^2 on left axis, 825-nm error on right), shown as function of depletion depth p_d for depletion profiles with different *vx* values. Depletions are relative to an F1 base model.

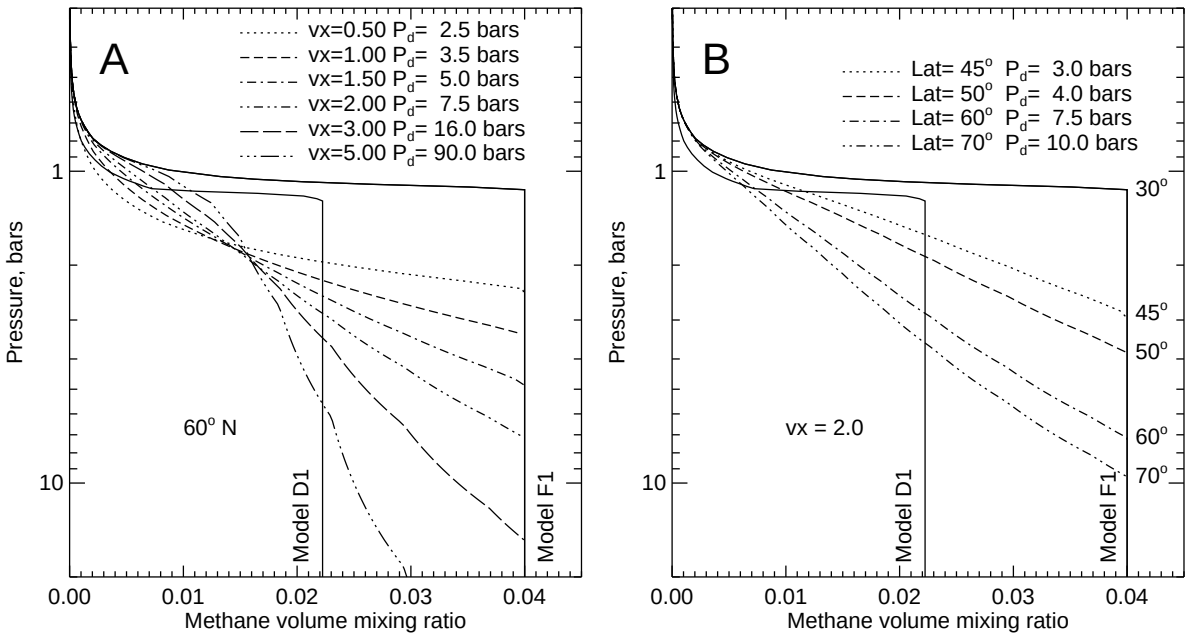

Figure 25: Depletion models for 60° N with different *vx* values (A) and best fit depletion models for different latitudes (B), assuming *vx*=2.0 for all latitudes.

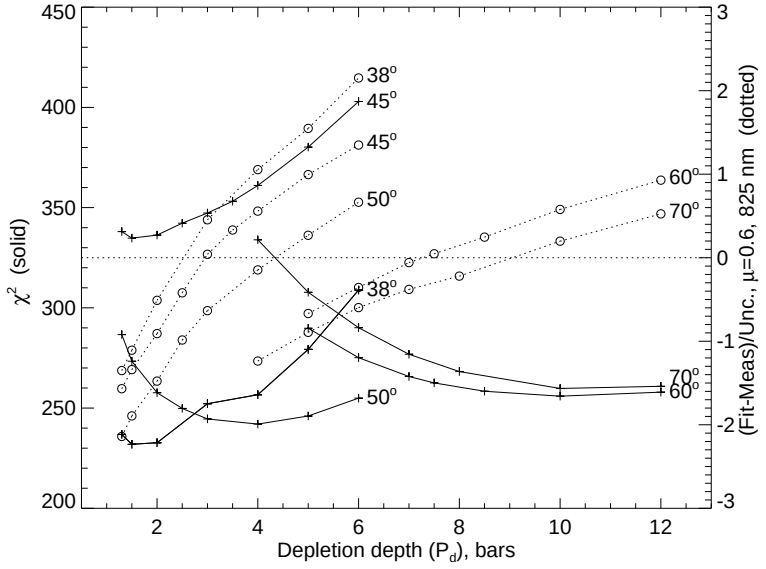

Figure 26: Fit quality estimates (χ^2 on left axis, 825-nm error on right) for compact cloud layer models versus depletion depth for depletion profiles with *vx* = 2.

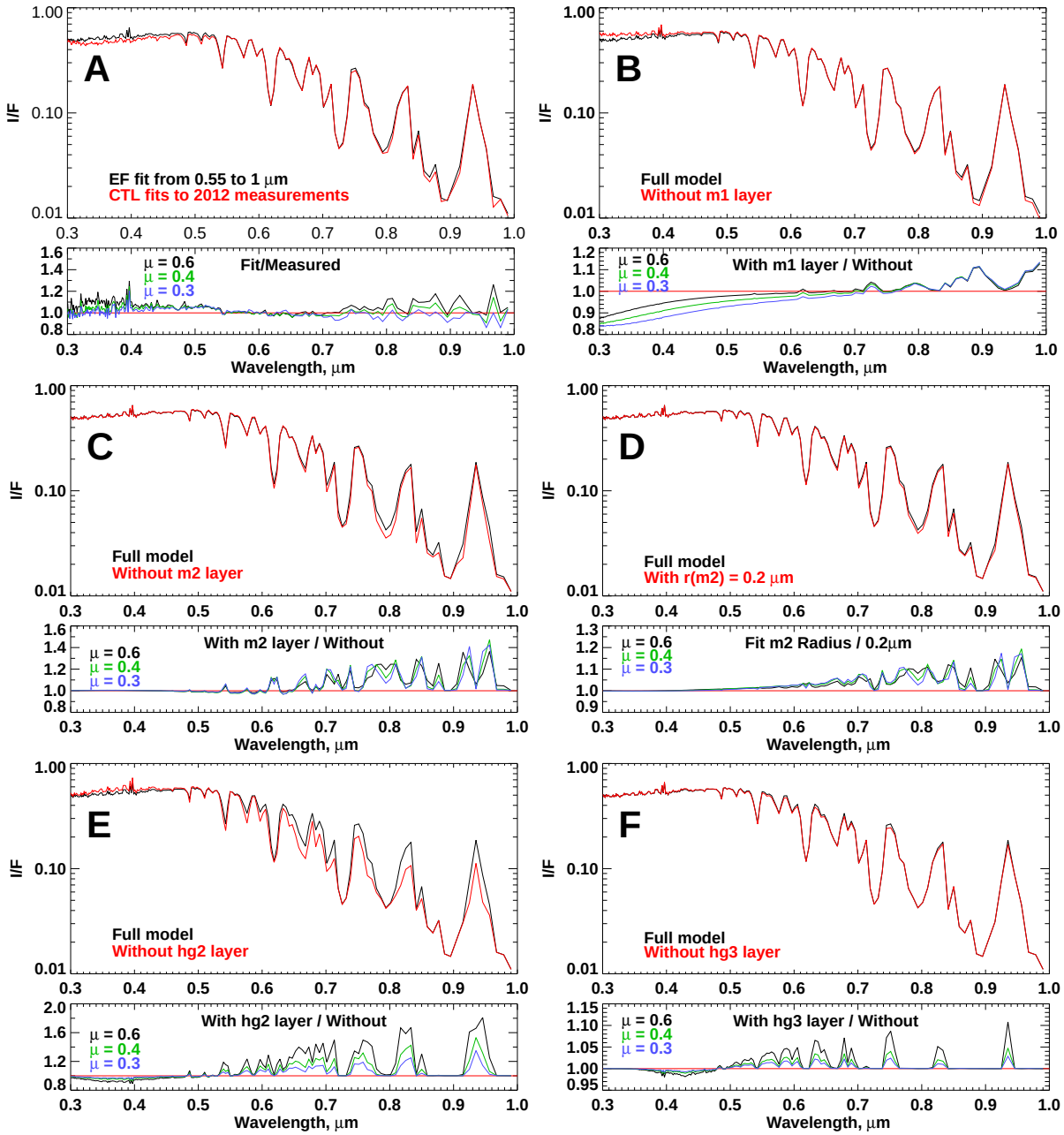

Figure 27: A: Comparison of measured STIS spectrum (red) at equator with a compact model fit (black) using the EF structure model, with spectra shown at a solar zenith angle cosine of 0.6 and ratios shown for all three cosine values); B-F: Comparisons of the model spectrum with spectra for same model with one aerosol layer removed or particle size changed (B: *m*1 removed, C: *m*2 removed, D: *m*2 particle radius reduced from 0.57 μm to 0.2 μm, E: *hg*2 removed, F: *hg*3 removed).

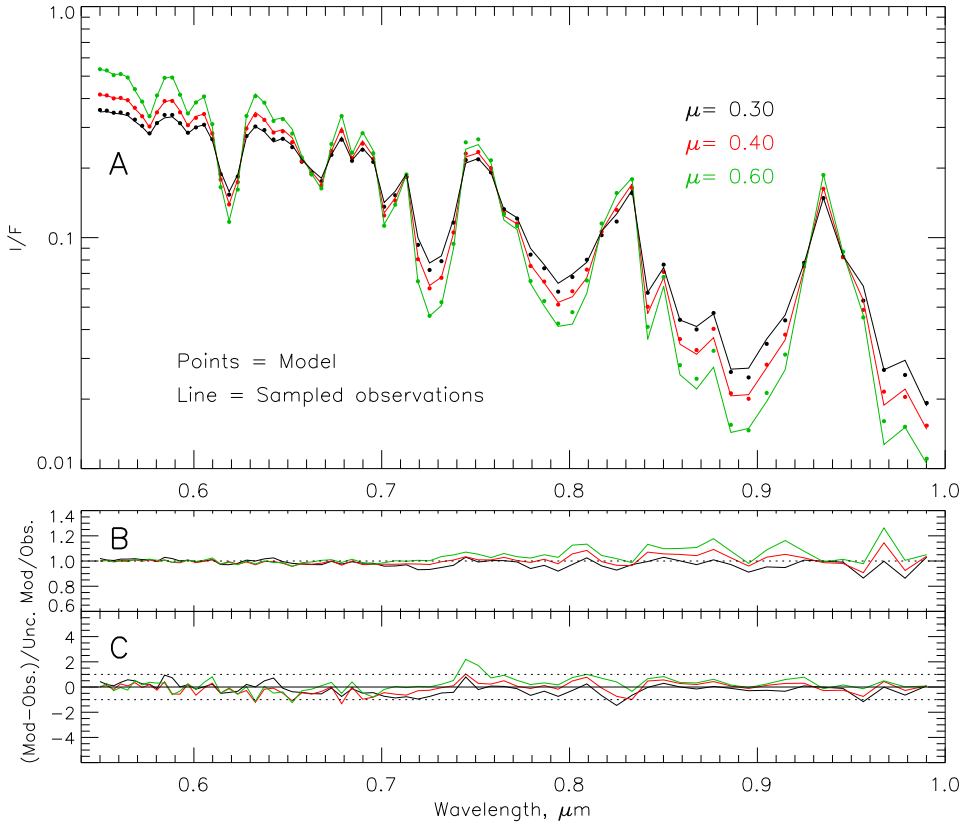

Figure 28: Comparison of model and measured spectra (A) at the equator, ratio of measured to model spectra (B) and difference spectra relative to expected uncertainty (C).

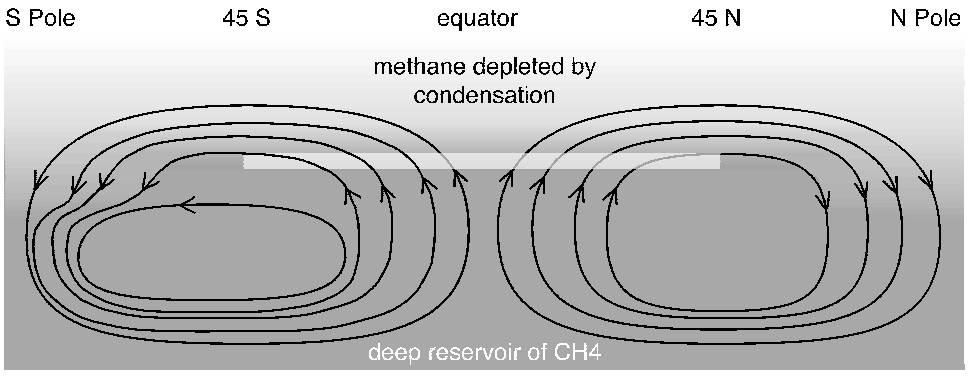

Figure 29: Speculative meridional flows in which rising flows at low latitudes produce methane condensation (white region) that depletes the gas of methane; the depleted gas is transported to high latitudes where it descends to reduce the mixing ratio at higher pressure. The depletion depth might be limited by the depth of the circulation, or by lateral mixing. A very deep cell of this type was suggested by (Hofstadter et al. 2007). The southern c ell streamlines provide shallower depletions at higher latitudes than the northern cell.

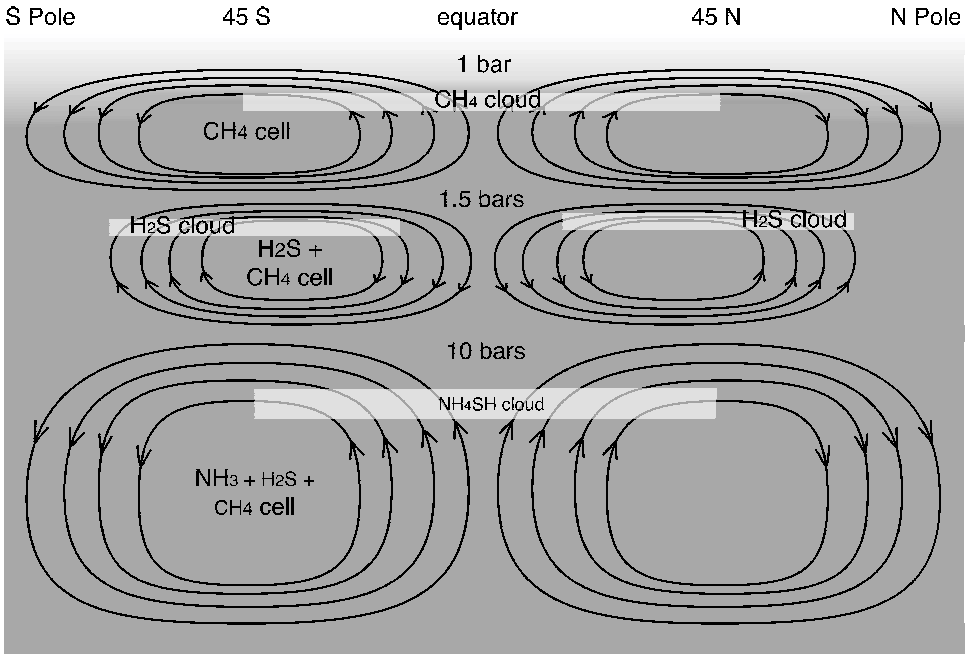

Figure 30: Speculated 3-layer cell structure providing equatorward flow at the berg level and poleward flow above methane condensation and NH_4SH cloud formation levels. Here cloud formation/condensation regions are indicated by light rectangles.